SMOX Gas Sensor Characterization of Classical Polycrystalline SnO_2 Materials at Room Temperature and Spectroscopic Analysis of Their Time Dependent Performance Degradation

Dissertation

der Mathematisch-Naturwissenschaftlichen Fakultät

der Eberhard Karls Universität Tübingen

zur Erlangung des Grades eines

Doktors der Naturwissenschaften

(Dr. rer. nat.)

vorgelegt von

Dipl. Chem. André David Sackmann

aus Tübingen

Tübingen

2025

Gedruckt mit Genehmigung der Mathematisch-Naturwissenschaftlichen Fakultät der Eberhard Karls Universität Tübingen.

Tag der mündlichen Qualifikation:	04.06.2025
Dekan:	Prof. Dr. Thilo Stehle
1. Berichterstatter/-in:	Prof. Dr. Udo Weimar
2. Berichterstatter/-in:	Prof. Dr. Günter Gauglitz

Table of content

I. List of abbreviations

LEL - Lower Explosion Limit

SMOX - Semiconducting Metal Oxides

TGS - Taguchi Gas Sensor

SMD - Surface-Mounted Device

LED - Light-Emitting Diode

RT - Room Temperature

DRIFTS - Diffuse Reflectance Infrared Fourier Transform Spectroscopy

ppm - parts per million

DC - Direct Current

DCR - DC Resistance

TCO - Transparent Conducting Oxide

TPD - Temperature Programmed Desorption

EPR - Electron Paramagnetic Resonance

IR - Infrared

PTFE - Polytetrafluoroethylene

GMS - Gas Mixing System

MFC - Mass Flow Controller

DMM - Digital Multimeter

EIS - Electrochemical Impedance Spectroscopy

MOX - Metal Oxide

RH - Relative Humidity

r.h. - Relative Humidity

1. Introduction

1.1 Motivation

An early use case, that necessitated the implementation of a gas sensor “device”, arose during the late 19th century. Hazardous gas atmospheres in coal mines were a lethal threat to unaware miners until John Scott Haldane suggested in 1895 the utilization of canaries as carbon monoxide detectors [1]. While attributes such as low energy consumption, room temperature operations and reliability were already met by this early gas warning system, other desirable attributes like miniaturization, lifetime, recoverability and warning radius were surely lacking. Alongside the Davy lamp which indicated the presence of methane or lack of oxygen by a change of its flame height, these early devices pioneered the ever-growing market of gas sensing [2].

Considered as the first modern era gas detectors, are catalytic combustion type sensors (LEL) first developed by O. Johnson while working for Standard Oil Co. of CA (now Chevron) in the 1920s. It helped improve safety at oil and gasoline storage sites by detecting critical levels of combustible gases. A Wheatstone bridge would measure the resistance change of a hot platinum wire in reference to a second filament (shielded from the gas stream).

In the medical field, methods to measure the oxygen saturation of blood were developed. In 1935 Karl Matthes could show that light of two distinct wavelengths would be absorbed by oxygenated hemoglobin and is therefore correlated with oxygen saturation [3]. Further improvement of the technique led to the developed of pulse oximetry in 1972 [4]. A different approach to oxygen analysis was taken by Leland C. Clark in 1953. He developed an electrochemical method to measure ambient oxygen partial pressure. A membrane allowed molecular oxygen to permeate into the electrode compartment holding a platinum cathode, where it is reduced [5].

Fundamental work for the establishment of semiconducting metal oxides as gas sensor materials was performed by W. Brattain and J. Bardeen in 1953, when they found direct evidence for gas sensitive behavior of germanium surfaces and could prove the presence of a space charge layer for this surface [6]. In the following year Heiland published his work on ZnO and its ability to change conductance by oxygen

absorption [7]. Other gas sensitive metal oxides where found in the following years by Bielanski (1957) and Seiyama (1962) [8] [9]. The first actual SMOX sensor device was patented by Taguchi (1962 in Japan, 1972 in USA) and used SnO_2 as a gas sensitive material [10] [11].

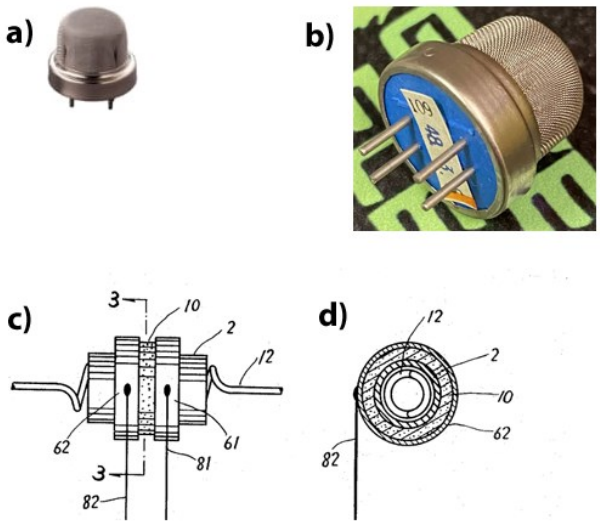

Figure 1: a) First commercially available SMOX-type gas sensor used in domestic environments as a town gas leakage alarm. Product name: TGS109 (Taguchi Gas Sensor). b) Side/bottom view of the same sensor showing the connector pins. Two pins connect the heater coil and another two connect the sensing electrodes. c) Schematic drawing (patent file) of the earlies gas sensing devices [11]. Notable components are the electrodes (61,62), the metal oxide layer (10) and the heater coil (12). d) Cut-through of the same device.

Modern day SMOX gas sensors in particular have certain properties that make them attractive for a wide variety of applications. Their working principle allows for very simple and low-cost sensor platforms, typically consisting only of a ceramic or silicon base plate equipped with electrodes and a heater wire. Covering the electrodes is a thin layer of gas sensitive metal oxide, which adds little to the overall bill of materials. Operation and read-out of such a sensor can easily be achieved with a set of simple and inexpensive electronics (Voltage source and voltage meter). Modern SMOX sensors with SMD packaging and integrated electronics are available for around 5 € (2500 pieces reel) making them a viable choice for sensors mesh network applications, low cost devices and even enable mobile phone implementation [12]. This is also promoted by the possibility to efficiently miniaturize such structures without suffering detrimental effects on sensor characteristics.

Applications where gas detection is critical or at least beneficial are plentiful and range from household appliances, over safety needs, to industrial process control.

Table 1: Overview on common applications for gas sensor systems

Gas sensor applications	
Indoor	Outdoor/Environmental
• Air quality monitoring • Air fresheners • Air purifiers • Ventilation control	• Weather stations • Pollution monitoring
Automotive	Safety
• Cabin ventilation control • Flap control • Hazardous vapor detection • Filter functionality monitoring	• Fire detection • Leakage detection • Personal gas monitors • Toxic/Flammable gas alarm
Food	Medical
• Packaging quality control • Food quality control • Cooking/baking process	• Breath analysis (Asthma) • Halitosis analysis • Disease detection
Industry	
• Process control • Fermentation control • Transistor oil monitoring	

It is generally accepted by the research community of SMOX gas sensing that unheated metal oxide layers of classical materials like SnO_2, WO_3 or ZnO perform poorly at ambient temperatures or basically any temperature below 150 °C [13]. While some materials may initially show respectable response to analytes even at low temperatures, it is usually short lived as ongoing baseline drift, degradation of response and sluggish response/recovery times increasingly plague the sensors' performance. Browsing through reviews of room temperature gas sensor publications, it can often be observed that the results shown focus mainly on selected gas cycles in idealized conditions, meaning freshly produced sensor, measured right after its initial temperature treatment and being exposed to its first gas cycles in purified air. While this approach is to be appreciated as an effort to discover potentially suitable materials for an analytical task at hand, it often times doesn't include analysis of crucial parameters that determine the suitability of a

sensor in real world applications. Surely one cannot expect every work to include measurement cycles in realistic air conditions as it does require sophisticated experimental setups, but more details on temperature history and stability over time would help to assess the suitability of the investigated material for continuous room temperature operation.

The advantages a stable room temperature gas sensor would bring to the table are plentiful. Without the need for a heating element, sensor substrate design would lose some complexity, further miniaturization would be enabled and production cost would decrease. Electronic components for heater operations would be void, hence reducing material and space requirements on the controller circuit, and further cost reduction. The absence of a heater would also remove the largest share of the sensors' overall power consumption, giving battery powered SMOX a significant boost in operation time. Applications with potentially explosive environments would be opened up to SMOX sensors, as it would no longer expose the gases to a hot surface.

Challenges presented by room temperature operation mainly relate to limited analyte gas signal strength and degradation of signals over time. Recovery tends to be slow or even incomplete. Strategies to tackle these draw backs are plentiful and range from tailor-made materials like graphene oxide [14], sulfides [15] and specific nanostructures [16], over light activation with LEDs [17], to miniaturization efforts with pulsed heating for recovery [18].

1.2 Review on low/room temperature gas sensing with SMOX

On the topic of basic understanding of RT gas sensing Degler contributed significant insights into the H_2O interplay on SnO_2. He performed H_2O/D_2O exchange experiments on tin dioxide in an operando DRIFTS setup and covered temperatures from RT to 400 °C [19]. The interpretation of the spectra at RT revealed a domination of associative adsorption of molecular water in form of physisorption and coordination to surface hydroxyl or oxygen groups. Water vapor also decreased the sensor resistance quite strongly, with the maximum decrease found to be at 150 °C and less pronounced towards 300 °C and higher. This was explained with reaching the onset temperature of oxygen ionosorption (referring to 150 °C), while water still acts as an electron donor but now has the means to displace ionosorbed oxygen. At even higher temperatures dissociative water

adsorption starts to dominate, while also partial desorption of hydroxyl groups occurs. The hydroxyl groups now regenerated by water dissociation are found to be part of a charge neutral reaction and therefore have low impact on the resistance.

Degler further investigated CO adsorption on a tin dioxide surface (sol-gel synthesis, 450 °C calcination in air), though be it at a temperature of 300 °C, it can provide a reference to the reaction taking place at RT. He observed decreasing OH bands upon CO exposure, both in dry and humid conditions. This is explained by a competition between CO and H_2O for reactive oxygen species, resulting in a lower OH coverage as CO is introduced to the gas mixture. Seemingly this would not occur in dry conditions, when CO is the only species looking for interaction with oxygen, though can be explained by the residual H_2O content of about 50 ppm in “dry air”. With the presence of CO, a decrease of Sn-O related bands is observed and its oxidation product is found in the appearance of CO_2 peaks centered around 2350 cm^{-1} associated with the two branches of the asymmetric stretch vibration of the molecule. No indication of intermediate reaction products, like carbonates or carboxylates can be found, even though other sources report the formation of those species on their investigated SnO_2 materials. The electronic impact the reaction with CO is explained by the creation of oxygen vacancies after CO_2 desorption which should be considered full ionized at 300 °C and release electrons into the conduction band. Re-oxidation will take place, but in equilibrium conditions the average oxygen coverage of the surface is still lower, than in absence of CO.

Very comparable spectra were recorded during exposure to H_2 (again at 300 °C) on the same sensor sample. Again, a decrease of hydroxy groups and Sn-O species were observed, pointing towards an oxidation of H_2 to form and desorb water.

A comprehensive review on materials explored for their room temperature gas sensing capabilities is provided by Li et al [20]. Sorted by the respective target gas, the following findings shall be highlighted:

Regarding H_2S sensing the most suitable metal oxide materials are found to be pristine ZnO [21], In_2O_3 [22], CeO_2 [23] and Fe_2O_3 [24]. The observed signals are linked to the ability of H_2S to form metal sulfur compounds even at RT which are

metallic conductors and thereby lower the electrical resistance considerably. Selectivity towards other analytes is good as these metal sulfides are not reactive to most other gases. On the other hand, recovery and re-oxidation are quite slow or even stay incomplete. Pulsed heating could be beneficial to achieve full recovery.

For H_2 sensing there are a number of material/preparation methods that show decent gas sensing properties at RT, but in most cases their sensitivity is lower than at higher working temperatures. Additionally, they are plagued by quite long response and recovery times or even a lack of capability to fully recover [25].

NO_2 is commonly detect best on SnO_2 [26], ZnO [27] or In_2O_3 [28] nanostructures. Sensor resistance on n-type semiconductors increases upon NO_2 exposure as it enhances oxidation of the surface. Synthesis routes yielding SMOX with a high content of oxygen vacancies tend to produce quite strong sensor signals to NO_2 at RT. Recovery times are reported to be within acceptable frames (few minutes) but little is shared about repeatability over a longer measurement period.

NH_3 appears to be well suited for RT detection and most of the commonly used metal oxides show sensitivity towards it [29]. Specifically, high surface area materials exhibit high signals with reasonable response/recovery times. Saturation effects, as NH_3 concentrations increase can become an issue but generally this doesn't seem to be an issue.

Most of the commonly used metal oxides also show sensitivity towards ethanol. Supposedly, ethanol is oxidized, even at RT, with surface attached molecular oxygen ions to form CO_2 and H_2O while releasing electrons into the conduction band. The commonly investigated ethanol concentrations are rather high (100ppm and more) but several nanostructured materials show strong and fast responses to this atmosphere [30] [31] [32]. A critical discussion on the viability of an oxidative reaction path of ethanol at RT is absent.

Decoration with noble metals, such as Pd [33], Pt [34] or Au [35], is commonly employed to improve gas sensing properties of SMOX materials and can be helpful to enhance the detection of gases like CO and H_2 which are generally considered harder to detect with pristine SMOX at RT. Especially at RT, where thermal energy is low, the chemical excitation provided by noble metals can enhance or even enable a specific gas sensitivity.

Examples – again found in the review of Li et al. – are Au decorated ZnO nanostars (signal of ~55, to 500 ppm CO) [36], Pd decorated ZnO nanowires [37] or Pt decorated SnO_2 nanostructures (signal of ~65, to 100 ppm CO) [38]. Even ultra-high H_2 responses are reported for Pd modified ZnO nanowires, achieving a signal of 13000 to 100 ppm H_2 [39].

About the sustainability of those excellent sensing properties at RT not much is told. Considerations of theoretically viable reaction paths in order to explain the strong responses and fast recoveries exclusively consider oxidation of CO or H_2 with surface oxygen without any backup of spectroscopic or otherwise gained evidence. Particularly, quick re-oxidation of the surface after the exposure event has ended, can be brought into doubt with everything that is known about oxygen adsorption behavior of SMOX at RT. An attempt should be made to properly explain such an ability to quickly re-oxidize and a direct link to the noble metal sensitization surely can help explain such phenomena.

1.3 Scope of the work

1.3.1 Previous work

Initial work on the topic was performed by myself within the frame of a diploma thesis [40]. Besides methodical challenges, like precise temperature control and repeatable sensor fabrication, it quickly became apparent that knowledge of each sensor's temperature history was crucial in order to explain strongly varying sensor behavior during identical tests. Freshly produced samples seemed to detect CO and H_2 at 25 °C quite well, whereas continued operation at 25 °C to 100 °C resulted in a complete loss of sensitivity after some days. In order to unify the results and allow for performance comparison between undoped and doped SnO_2 samples, all sensors underwent a prolonged storage at RT after they had been initially calcinated. Only then were they measured at increasing temperatures from RT to 100 °C.

In this state, the undoped variants showed no response to the target gases at any temperature below 100 °C and even then, just minor signals. The Pd doped variant of SnO_2 calcined at 1000 °C was able to slightly enhance H_2 signals at 100 °C operating temperature, but no other positive effect could be observed for lower temperatures or for CO exposure. The SnO_2 variant with Pt doping provided a clear enhancement in basically all temperatures and gases tested.

In summary none of the tested variants showed noteworthy signals to CO and H_2 when stored for several days and then operated at room temperature.

1.3.2 Scope of this work

This work is aiming to take a closer look at the processes and sensor characteristics occurring in the sub-150 °C temperature regime, while trying to show possible benefits and possibilities when tapping into this underestimated domain of SMOX gas sensing.

Tin dioxide was selected as the main material for all investigations and research. Out of a common synthesis route, two base materials were synthesized and additionally two precious metal additives (Pd and Pt) were applied per base. The choice for tin dioxide roots in its thoroughly established position in SMOX research as well as its utilization in commercial products. It is arguably the most investigated classical material and allows the upcoming findings to be integrated into the bigger picture.

Regarding the selection of analyte gases, key criteria were simplicity of the available reaction routes and the ability to produce a sensor response at RT in the first place. Factors such as relevance and demand for commercial use were considered but had lower weight in the decision. Carbon monoxide was the obvious first choice. Its ability to be oxidized without the need for a preceding splitting of the molecule, makes it stand out within the list of candidates. Hydrogen was selected as well, due to its simple structure and the way it can be activated by Pd and Pt, hereby opening up a potential for detection at room temperature. For both gases a number of industrial applications exist and respective sensor modules are available from every major sensor manufacturer.

Besides basic characterization of the selected sensor materials with the help of DC measurements, a focus was put on temperature and time dependent degradation of the sensor signals to CO and H_2 and on the potential reversibility of that phenomena.

Complementary operando DRIFTS/DCR measurements were performed to gain a better understanding and deeper insights into the chemical changes of the metal oxide surface at RT. The test sequence included a high temperature phase with

test gas exposure followed by an abrupt cool down to RT and continued recording of DCR and DRIFTS spectra for several days.

Linking the insights gained by Degler et al. [19] on humidity influence of tin dioxide at RT with the here performed measurements, a more complete picture of the interactions of H_2O, O_2 and the test gases CO and H_2 is given.

Further investigations on O_2 adsorption and desorption behavior of SnO_2 at RT were conducted and analyzed. The sensors were exposed to dry nitrogen at a temperature of 400 °C for several hours before they were cooled down to the respective temperature of interest. After some hours at the target temperature (and still in N_2 atmosphere), rising concentrations of O_2 were introduced to the gas mixture and subsequently removed again.

The final set of experiments present here revolved around the immense potential in selective gas sensing, utilizing the help of a temperature modulation between RT and 400 °C. The presented temperature ramps were deliberately chosen to be slow paced, meaning while not viable for direct adaptation into a commercial product, they allow for proper analysis of the transient and equilibrium states of each temperature step.

2. Basic aspects of tin dioxide based gas sensors

2.1 Material properties of tin dioxide

Cassiterite is the world's primary tin ore up until today as it contains up to 78.8% tin. In its crystalline form tin dioxide (stannic oxide) is part of the rutile group and features tetragonal symmetry with a quadratic base of a = b = 4.737 Å, a height of c = 3.185 Å. Its space group is $P4_2/mnm$ with each tin atom being surrounded by six oxygen atoms in a distorted octahedral shape and each oxygen neighboring three tin atoms [41]. Within the unit cell, tin cations are positioned at (0,0,0) and (½,½,½). Oxygen anions at ±(u,u,0) and ±(½+u, ½-u, ½) with u = 0.307 [42].

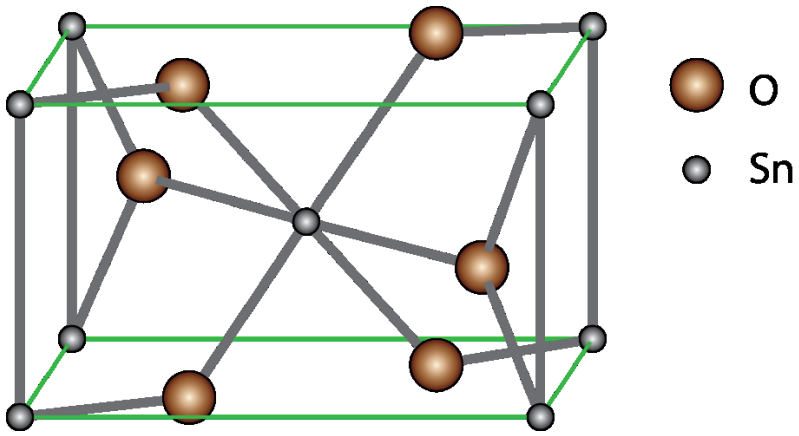

Figure 2: Unit cell of pristine SnO_2 with 6-fold coordinated Sn^{4+} and 3-fold coordinated O^{2-}.

Without any defects, meaning in its stoichiometric form, SnO_2 has to be considered a wide band-gap insulator (3.6 eV) [43] but due to presence of multivalent Sn(IV) and Sn(II) the formation of oxygen vacancies has a quite low energy barrier and thereby induces n-type semiconductor properties for non-stoichiometric SnO_2. These vacancies are considered to be singly or doubly ionized and act as electron donors to the conduction band.

The initial ionization energy levels for SnO_2 are situated at 30 meV and 150 meV below the conduction band, respectively [44]. The concentration of these defects depends on temperature and increases as the temperature rises. Composition of the gas atmosphere and partial pressure of oxygen further influence the level of decomposition of SnO_2 into SnO and O_2. This phenomenon elucidates the influence of various preparation techniques (such as powder calcination and layer annealing)

on the material's properties. It also provides insight into the drift observed in sensors used under varying temperature and oxygen concentration conditions [45].

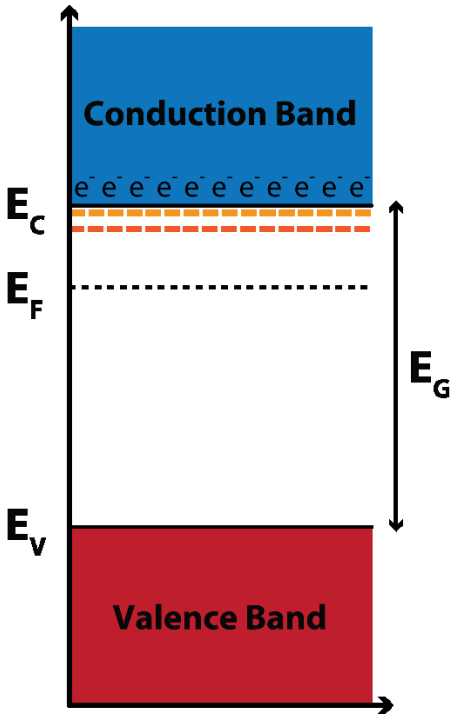

Figure 3: Schematic of the energy band diagram of tin dioxide. Its band gap (E_G) is 3.6 eV wide with two donor levels near the conduction band. These result from oxygen vacancies and are located at 30 meV and 150 meV.

The characteristic of SnO_2 extends its applications beyond serving as a solid-state gas sensor material. It finds widespread use as a transparent conductor (known as TCO) for electrodes in devices like solar cells, light-emitting diodes, and flat panel displays [46]. However, its transparency is limited to the visible spectrum, and it exhibits high reflectivity for infrared light. Consequently, SnO_2 is an excellent choice for window coatings that facilitate heat exchange with the surroundings while allowing the transmission of visible light [47].

In terms of surface properties, SnO_2 acts as an oxidation catalyst in its own right. According to the Mars-van-Krevelen mechanism [48], the multivalence of tin makes it easy to undergo surface reduction and reoxidation processes. As a result, lattice oxygen readily dissociates to react with adsorbed molecules. The various adsorption and reaction steps involved in its use as a gas sensor will be elaborated upon in the next chapter.

2.2 Surface reactions with selected molecules

The crucial role of surface oxygen species in catalytic and gas-sensitive properties of SnO_2 has been a subject of controversy in recent decades. Various molecular species, such as superoxo (O_2^-) and peroxo (O_2^{2-}), as well as atomic species like atomic radicals and closed valence shell oxides, have been proposed to exist on the SnO_2 surface [49]. These species are viewed as intermediates in the transformation of atmospheric oxygen to lattice oxygen (Reaction 1). A sequence of reactions can be proposed, assuming each reaction involves the transfer of one electron and the formation of neutral, mono, and doubly negatively charged oxygen species. The following proposal simplifies the reaction steps by disregarding the role of surface sites and oxygen vacancies. Initially, atmospheric oxygen is adsorbed as an uncharged molecular species (Reaction 2), which then captures electrons from the solid, resulting in the formation of a superoxide (Reaction 3). Subsequently, a peroxide is formed (Reaction 4). Following this, molecular oxygen dissociates into two atomic species (Reaction 5), which, upon abstracting additional electrons, become incorporated as lattice oxygen on the surface layer of the metal oxide (Reaction 6) [50] [51].

$\frac{1}{2}O_{2,gas} + V_O^{2+} + 2e^- \leftrightharpoons O_O$	**Reaction 1**
$O_{2,gas} \leftrightharpoons O_{2,ads}$	**Reaction 2**
$O_{2,ads} + e^- \leftrightharpoons O_{2,ads}^-$	**Reaction 3**
$O_{2,ads}^- + e^- \leftrightharpoons O_{2,ads}^{2-}$	**Reaction 4**
$O_{2,ads}^{2-} \leftrightharpoons 2O_{ads}^-$	**Reaction 5**
$O_{ads}^- + e^- \leftrightharpoons O_{ads}^{2-} \leftrightharpoons O_O$	**Reaction 6**

Considering theoretical calculations regarding the adsorption of oxygen on SnO_2 (110) and (101) surfaces, the most stable molecular species can be assumed to be the superoxide species, while the most stable atomic species is the lattice oxygen, specifically the twofold coordinated bridging oxygen [52]. Experimental verification of various oxygen species primarily relies on three techniques: Temperature Programmed Desorption (TPD), Electron Paramagnetic Resonance (EPR), or IR spectroscopy. TPD investigations reveal three prominent desorption peaks, corresponding to molecular oxygen, atomic oxygen, and material decomposition,

respectively [53]. The presence of these oxygen species is heavily influenced by the sample's pre-treatment. EPR spectroscopy identifies the first desorption peak, occurring between 100 and 200 °C, as singly charged molecular oxygen (superoxide) [54]. IR spectroscopy confirms the existence of superoxide in reduced SnO_2 samples [55]. The second desorption peak, occurring at around 600 °C, is attributed to atomic oxygen [53]. Unlike molecular oxygen species, atomic oxygen species cannot be observed through IR spectroscopy. Beyond 750 °C, the metal oxide undergoes decomposition as lattice oxygen starts to desorb [53]. Lattice oxygen within the metal oxide remains present at temperatures pertinent to gas sensing, but its reactivity may vary depending on temperature and differ between surface and bulk lattice oxygen. Experiments involving $^{16}O_2$-$^{18}O_2$ exchanges on pristine SnO_2 indicate that bulk oxygen exchange occurs above 425 °C [56].

Adsorption of Water

Water on SnO_2 surfaces exists either as molecular species or as hydroxyl groups. Molecular adsorption encompasses both physisorbed (Reaction 7) and associatively adsorbed/hydrogen-bonded water molecules (Reaction 8). In the case of dissociative adsorption, the formation of hydroxyl groups necessitates an additional oxygen atom to maintain reaction stoichiometry, as proposed by S. R. Morrison for the dissociative adsorption of water on oxide surfaces (Reaction 9) [57]. Various experimental studies indicate that molecular water is detectable up to 200 °C, while hydroxyl groups, signifying dissociatively adsorbed water, persist above 500 °C, albeit diminishing notably around 300-400 °C [55] [58] [59]. The temperature programmed desorption (TPD) profile of water adsorbed on SnO_2 reveals two desorption peaks centered at 100 and 400 °C. The lower temperature peak corresponds to the desorption of molecular water, completing around 200 to 250 °C. The recombination of surface hydroxyl groups initiates the second desorption peak at 250 to 300 °C [60]. TPD findings align well with infrared spectroscopic observations, which note the desorption of physisorbed water up to 150 °C and a significant decline in surface hydroxyls above 200 °C [61].

$H_2O_{gas} \leftrightharpoons H_2O_{phys}$	**Reaction 7**
$H_2O_{gas} + O_O \leftrightharpoons HO \cdots H \cdots O_O$	**Reaction 8**
$H_2O_{gas} + O_O + S \leftrightharpoons (OH)_O + (OH)_S$	**Reaction 9**

Several models have been proposed to explain the electrical impact of water vapor through dissociative adsorption. The reactions presented above are oversimplified, neglecting the nuances of surface characteristics and the attachment of oxygen and hydroxyl species. Generally, water exhibits a reducing effect on SnO_2, attributed to various mechanisms. The first mechanism involves the generation of an oxygen vacancy and two hydroxyl groups bonded to Sn, termed terminal hydroxyl groups. This reduction occurs due to the ionization of the oxygen vacancy (Reaction 10). The second mechanism leads to the creation of one terminal hydroxyl group and one attached to multiple Sn atoms (Reaction 11), known as rooted hydroxyl groups, which are also regarded as donors [50]. Another reaction between water vapor and the SnO_2 surface results in the formation of two rooted hydroxyl groups through the interaction of surface oxygen, a surface oxygen vacancy, and a water molecule (Reaction 12) [62]. Although this reaction yields hydroxyl groups, it does not affect the material's conductivity.

$H_2O_{gas} + O_O + 2Sn_{Sn} \leftrightharpoons 2\left(Sn_{Sn}^{\delta+} - OH^{\delta-}\right) + V_O^{2+} + 2e^-$	**Reaction 10**
$H_2O_{gas} + O_O + Sn_{Sn} \leftrightharpoons \left(Sn_{Sn}^{\delta+} - OH^{\delta-}\right) + (OH)_O^+ + e^-$	**Reaction 11**
$H_2O_{gas} + V_O^{2+} + O_O + Sn_{Sn} \leftrightharpoons 2(OH)_O^+$	**Reaction 12**

The reducing effect of water can be explained by considering both dissociative and associative adsorption. In models of associative adsorption, water molecules interact with acidic or basic surface species [57] [63] altering their electronic states, or they inhibit oxygen adsorption by competing for the same sites [64]. Theoretical studies on stoichiometric, reduced, and oxidized SnO_2 (110) surfaces have evaluated the stability and electronic effects of both associative and dissociative adsorbates [65]. Specifically, associative adsorption (Reaction 8) involves water molecules donating electrons to the SnO_2 surface, making them weak electron donors. In contrast, during dissociative adsorption, electrons are transferred from surface or bridging oxygen atoms to the terminal hydroxyl groups. This transfer compensates for the initial electron donation seen in associative adsorption, resulting in little net change in resistance.

According to the model, the reducing effect of water vapor arises either from dominant associative adsorption or from the formation of oxygen vacancies. However, this theoretical approach may not fully capture the complex processes on polycrystalline SnO_2, which features various facets and defects. Furthermore, calculations reveal that the balance between associative and dissociative adsorption is strongly affected by surface stoichiometry – particularly oxygen coverage – and by the presence of pre-existing dissociated water, such as hydroxyl groups [65]. Experimental results on variously prepared (110) surfaces support these findings, showing that surface stoichiometry significantly impacts dissociative water adsorption [66]. Similar trends have also been observed on the (101) surface in both theoretical and experimental studies [67].

In summary, both experimental and theoretical studies demonstrate that water adsorption – and the resulting electronic effects – are highly dependent on temperature, surface composition, stoichiometry, and the presence of hydroxyl groups.

Adsorption of Carbon Monoxide

Exposure of SnO_2 to CO was studied by a number of publications and specifically IR spectroscopic investigations identified the formation of carbonate and carboxylate species [59] [68] [69] [70]. Both unidentate and bidentate variants are reported for either variant up to temperatures of 400 °C [59], although a significant influence of sample calcination and pre-treatment procedure was reported [68]. Supposedly, at room temperature bicarbonate species exist, though spectroscopic proof appears challenging as even deuteration failed to allow for a clear assignment [69]. Theory provides a number of reaction pathways, explaining the formation of said carbonate and carboxylate species upon interaction of CO with surface oxygen [69]. On a (110) surface they indicate carbonate formation when CO interacts with molecular oxygen occupying an oxygen vacancy (Reaction 13). Carboxylates on the other hand involve lattice oxygen of a reduced surface (Reaction 14) [71]. Similar results were observed for the (101) surface. Theoretical calculations indicate the presence of a carboxylate-like intermediate during the reaction between CO and lattice oxygen (Reaction 14), leading to the desorption of the intermediate and the formation of an oxygen vacancy (Reaction 15) [52]. In contrast, the formation of carbonates on the (101) surface is suggested by

calculations to involve a reaction between CO_2 and lattice oxygen (Reaction 16) [52].

$CO_{gas} + O_{2,ads}^{\alpha-} + (2-\alpha) \cdot e^- \leftrightharpoons (CO_3)^{\alpha-}$	**Reaction 13**
$CO_{gas} + O_O \leftrightharpoons (CO_2)_O$	**Reaction 14**
$(CO_2)_O \leftrightharpoons CO_2 + V_O^{2+} + 2 \cdot e^-$	**Reaction 15**
$CO_{2,gas} + O_O \leftrightharpoons (CO_3)_O$	**Reaction 16**

The reversible adsorption of CO_2 as carbonates or the decomposition of carbonates formed by a reaction with CO is not expected to significantly alter the electronic properties of the solid. However, the decomposition of carboxylates formed by CO results in the creation of an oxygen vacancy, which can donate electrons to the solid. The formation of carbonyl species (Reaction 17) on pristine SnO_2 materials has only been observed for CO adsorption at 120 K [72]. Theoretical calculations suggest that the electronic effects of CO adsorption are much smaller than those caused by the formation of an oxygen vacancy [52] [71].

$CO_{gas} \leftrightharpoons CO_{ads}$	**Reaction 17**

The surface species discussed above are summarized in Figure 4. For surface oxygen, only species confirmed through experimental techniques are included. It is important to note that, with a few exceptions, the experimental conditions – such as temperature, pressure, atmospheric composition, and sample form – differ significantly from the actual operating conditions of gas sensors. A more detailed summary, including the corresponding experimental techniques, is available in [49].

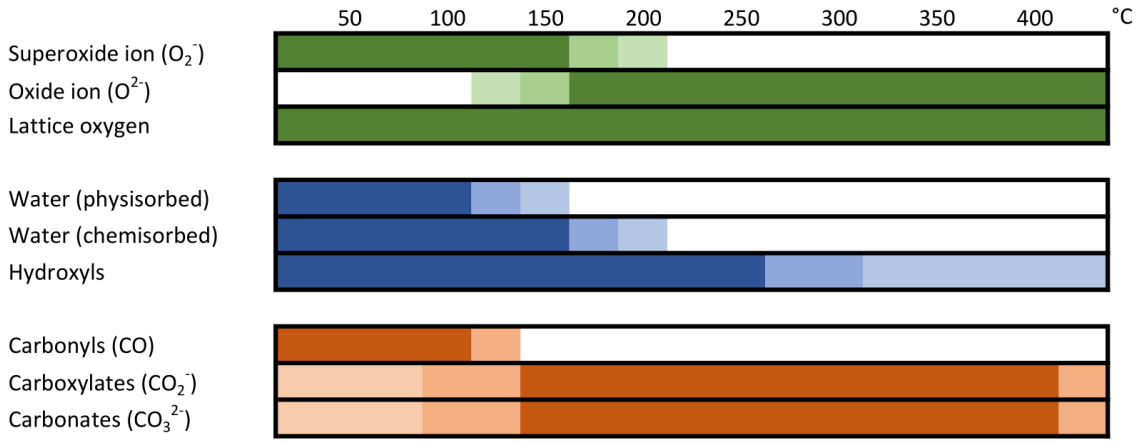

Figure 4: Summarized temperature dependence of surface species identified on SnO_2 by EPR, TPD and IR techniques. Color intensity indicates the incidence of a species at a given temperature. The figure was adapted from [49] and [73].

Absorption of hydrogen

Another gas of major interest was hydrogen. Despite being non-toxic, its combustibility and its use for all sorts of applications, makes it a crucial analyte in the gas sensor world. Hydrogen is additionally a fairly simple molecule and can therefore provide useful insights into the understanding of fundamental operation principles of sensors.

There are a number of similarities between H_2 and the previously discussed CO molecule. Due to their simple structure, both have limited possibilities for reaction paths to take. Both thermodynamically favor an oxidation reaction where $H_2 + ½O_2 \leftrightharpoons H_2O_{gas}$ yields $\Delta H_R = -242kJ \cdot mol^{-1}$ and $CO + ½O_2 \leftrightharpoons CO_2$ yields $\Delta H_R = -286kJ \cdot mol^{-1}$ [74].

At elevated temperatures the following reactions of hydrogen on a SnO_2 surface have been established:

$½H_{2,gas} + O_O \leftrightharpoons (OH)_O^+ + e^-$	**Reaction 18**
$H_{2,gas} + O_S^- \leftrightharpoons H_2O_{gas} + e^- + S$	**Reaction 19**

Described in Reaction 18 is the formation of rooted hydroxyl groups by oxidation of H_2 with lattice oxygen. Although this path should release an electron into the conduction band, M. Hübner [75] postulates that in an oxygen containing

atmosphere (and sufficient thermal energy) the electron will instead find its way to the acceptor levels of adsorbed oxygen followed and is consumed by further adsorption of atmospheric oxygen. The net conductance change is therefore zero and a downward band bending (or reduction of pre-existing upward band bending) is not induced.

Reaction 19 on the other hand, describes hydrogen interacting with ionosorbed surface oxygen resulting in the formation of water and ultimately a vacant surface site. In this scenario released electrons will increase the number of free charge carriers in the conduction band and lead to a lowering of the band bending, in turn explaining the decrease of resistance [75].

2.3 Surface decoration with noble metals

Even in their pristine form many metal oxides already show some level of gas sensitivity. While this may be true, there is typically still room for improvement especially concerning response and recovery time, stability and the possibility to alter gas selectivity. This is where noble metals decoration or loading comes into play. Generally, these additives will influence the gas reception and can additionally alter the transduction function of the material [76] [77]. Alternatively to surface loading, noble metals can be incorporated into the metal oxide lattice if utilized appropriately during synthesis and calcination. However more commonly and often more effectively, additives are applied as surface loadings, creating a separate phase atop the pristine metal oxide particles (inhomogeneous dispersion). The associated mechanisms of sensitization are currently considered to be either of chemical nature, translating to a spill-over of affected gases to the metal oxide base [78] or alternatively a sensitization of electronical nature, which originates from the influence of the additive's fermi-level on the energy bands of the base material [76] [77]. The afore mentioned spill-over mechanism involves absorption, activation and transfer of relevant gases like oxygen, carbon monoxide, hydrogen or other reducing gases. The activation step may involve weakening or even fully dissociating intramolecular bonds while gases are adsorbed on the metal clusters. Upon transfer of activated species to the metal oxide host, effectively an increase of gas reactivity is obtained.

3. Material synthesis and sensor fabrication

3.1 Tin dioxide synthesis

SnO_2 powder is readily available from most chemical companies at various purity levels and particles sizes. The lack of control over many parameters relevant for an application as a gas sensitive layer, necessitates an in-house preparation route. This allows for selective sourcing of chemicals, choice of synthesis route and full control over the calcination and milling aspects.

The selected synthesis route was an aqueous sol-gel process with $SnCl_4$ as the main component and tin source [79] [80]. $SnCl_4$ was sourced from Sigma-Aldrich (99.995 % purity) and used to prepare a 2M aqueous solution. To avoid premature hydrolysis, an ice-bath was used to keep the temperature of the solution below 5 °C at all times, while adding $SnCl_4$ dropwise. In a similar fashion, a 2M aqueous ammonia solution was prepared (Merck EMPROVE 25 %) in a three-neck round-bottom flask and cooled down in a salt-ice-bath. As soon as 0 °C were reached, dropwise addition of the $SnCl_4$ solution commenced and temperature was constantly monitored to stay between 0 °C and 5 °C. A strong KPG® stirrer with PTFE propellers was needed to keep the solution well mixed as gelation continuously increased its viscosity. After completely mixing the two solutions the ice-bath was removed and stirring continued for an hour. The obtained suspension was then transferred to centrifuge tubes (Falcon) and after initial centrifugation (200 rpm for 15 minutes) the white precipitate was washed several times with deionized water and centrifuged again. Each run was checked for chloride content by adding $AgNO_3$ to the separated liquid phase. The resulting product was unified in a large diameter petri dish and dried in an oven at 80 °C for 48 hours.

After drying the product took the shape of hard, glass-like crystals of varying size (few millimeters to one centimeter). After some initial grinding in a mortar the coarse powder was placed in an 80 ml ZrO_2 grinding jar and 5 mm ZrO_2 balls were added. For this milling step, no liquid or binder of any form was added. A planetary ball mill (Fritsch “Pulverisette 5”) was used and set to 150 rpm for 2 hours. The resulting fine, white powder was split up on two alumina crucibles and then one was calcined at 450 °C for 8 hours and the other at 1000 °C for 8 hours in a Nabertherm GmbH R 50/250/13 tubular furnace. The calcined powders were milled again using 5 mm balls, deionized water as a binder and 200 rpm speed for 2 hours. After a final

drying step at 80 °C, the pristine form of SnO_2 450 °C (labeled IPC450) was received as a yellowish powder and pristine SnO_2 1000 °C (labeled IPC1000) as a white powder. A summary of the whole process is shown in Figure 5.

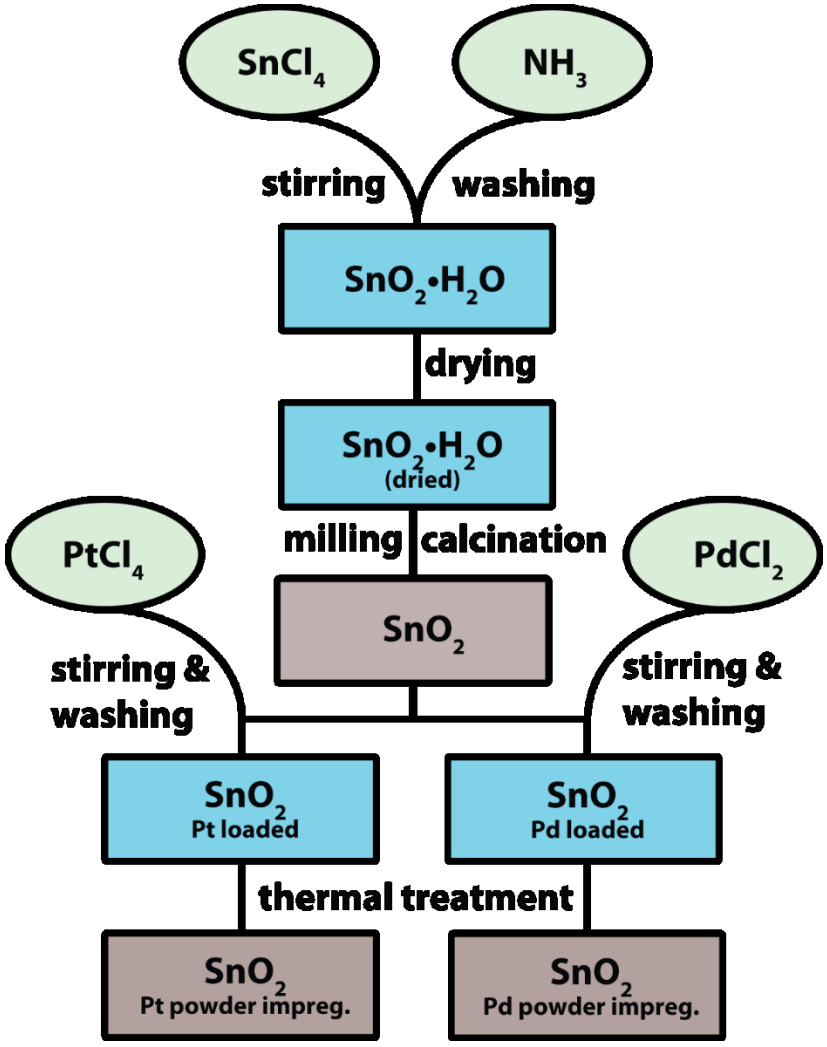

Figure 5: Schematics of synthesis route for pristine and powder impregnated SnO_2. Calcination of pristine SnO_2 was performed at 450 °C and 1000 °C for 8 hours. Thermal treatment of loaded SnO_2 was done at 450 °C for 1 hour.

3.2 Decoration of tin dioxide

Noble metal decoration was achieved through the impregnation of SnO_2 powder, as illustrated in Figure 5. $PtCl_4$ or $PdCl_2$ (Merck/Sigma-Aldrich, 99.99% trace metal basis) was used to prepare an aqueous base solution, which was acidified with a few drops of HCl. Stoichiometric amounts of the base solution were added to SnO_2 powder dispersed in water, resulting in nominal loadings of 2.0 wt.% Pt and Pd. After stirring the mixture for 48 hours at room temperature, it was centrifuged, and the obtained solid was redispersed in bi-distilled water (centrifuge flasks filled to 50 ml) for washing. This washing process was repeated three times, after which the

solid was dried overnight at 80 °C. Finally, the material underwent heat treatment at 450 °C for 1 hour in an alumina vessel (Nabertherm R 50/250/13).

3.3 Sensor fabrication

The sensing layers were deposited by screen-printing a propylene glycol-based paste of the sensing materials onto a sensor substrate, which was equipped with interdigitated electrodes on the front and a heating meander on the back (see Figure 6). For this work the majority of produced sensors used substrates with Pt electrodes and heaters. Only a short measurement campaign was performed on substrates with Au electrodes and a heater made from Pd/Ag alloy.

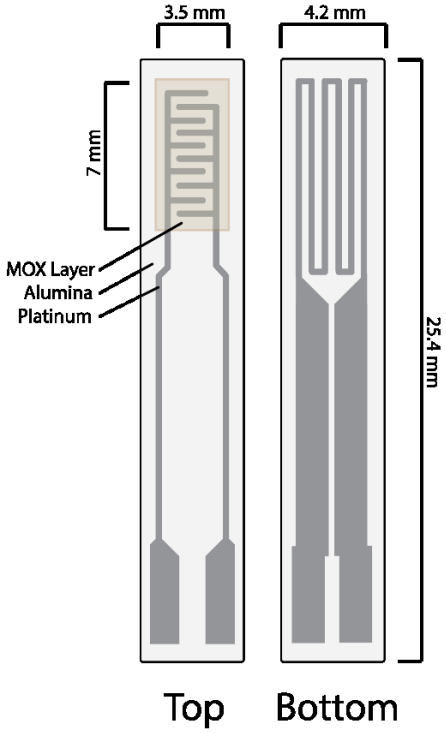

Figure 6: Schematics of a ceramic sensor substrate fitted with platinum electrodes on its top side and a meander heater on the back. The gas sensitive layer is screen-printed atop the electrode area with a thickness of about 50 µm. The platinum structures themselves have a thickness of 5 µm.

After printing the sensors were dried at 80 °C for at least 24 hours and annealed at stepwise varied temperatures (300 °C – 400 °C – 500 °C – 400 °C – 300 °C) and a step duration of 10 minutes. For each individual sensor a temperature calibration was established by plotting the temperature of the sensing layer (measured with an infrared pyrometer) versus the resistance of the heater. Based on the linear relation between layer temperature and heater resistance the sensor can be precisely heated during the experiments. Utilizing the heater resistance instead of the heater

voltage as a means to set the sensor temperature has the advantage of compensating for potential cooing effect by applying an air flow or the additional heat generated by sensor being mounted in a tight sensor chamber (heat up of the chamber walls).

4. Experimental setups

4.1 Gas mixing systems

Ensuring absolute control over the composition of gas mixtures is crucial for any gas sensor related research. Even more care has to be taken when investigating oxygen free and water free atmospheres as even small leakages and impurities can cause deviations from the desired composition. The general makeup of such a gas mixing system (GMS) consist of a number of gas channels, each containing a gas inlet port connected via Teflon tubing and Swagelok fittings to a mass flow controller (MFC), followed by a magnetic valve and finally leading into a common gas line which feeds the sensor chamber with the desired gas mixture. The first two channels are typically connected to a carrier gas bottle (synthetic air or pure N_2) with one of them being equipped with a water vaporizer in-between the MFC and the magnetic valve. Additional channels are usually hooked up to pre-diluted analyte gas bottles (in a background of the selected carrier gas). All gas bottles were supplied by Westfalen AG Münster and had a purity of 99.9999% for nitrogen and synthetic air. Analyte gas bottles came with certified concentration analysis performed by the supplier. Deionized water was sourced from our building's ion-exchange system and then poured into the vaporizers.

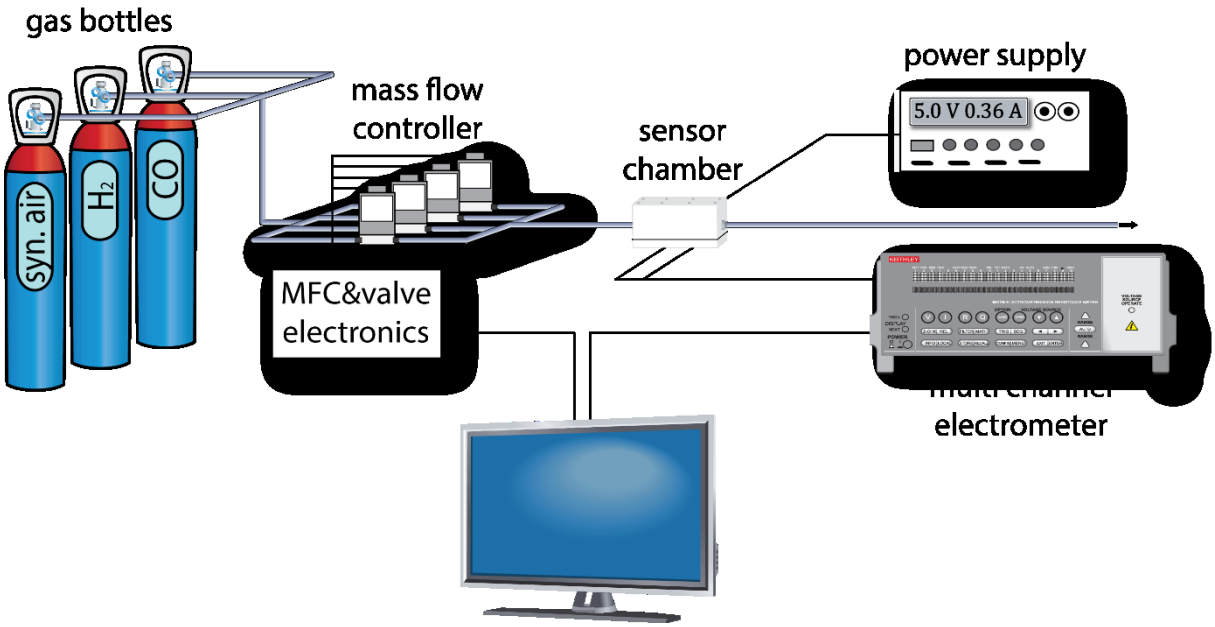

Figure 7: Gas mixing system with attached DC resistance measurement equipment. Computer software sets and controls the flow rate of each mass flow controller and logs the output of the electrometer.

In this work a total of three different gas mixing systems were configured and utilized. One system was dedicated to less demanding gas mixtures, but incorporated the ability to pre-flush each test gas channel to ensure fast and smooth transitions to the subsequent gas composition. This helps to avoid initial overshoots or the accumulation of contaminants in gas channels. The majority of sensor tests took place in this gas mixing system (GMS).

The second system consisted exclusively out of stainless steel tubing with special fittings to maximize gas tightness. Any measurement in pure nitrogen as a background gas and/or the absence of humidity was performed in this system. Residual oxygen concentrations were determined to settle below 1 ppm. Water was measured at around 10 ppm which reflects the quality of the used N6 purity nitrogen bottles.

System number three was used in conjunction with the IR spectroscopy setup and had a regular 6 MFC configuration allowing for the dosing of up to 4 analyte gases in a background of humidified air.

4.2 DC resistance setup

Direct current (DC) resistance measurements represent the fundamental method to investigate and operate SMOX-based gas sensors. An investigative setup consists of a gas mixing system to deliver at constant flow rates the desired gas mixtures, at least one sensor chamber containing the investigated sensors, a resistance readout device (Digital Multimeter Scanner Keysight E34972A or Keithley 199), a voltage source to power the sensor heaters (HP, Keithley, Korad models used) and a reference gas sensor module to monitor gas temperature, humidity and general functionality of the GMS.

The DMM Keithley 199 was used to record the sensor resistance while performing operando IR spectroscopy (DRIFTS setup described in the subsequent chapter). In its highest resistance range the device can measured up to 300 MΩ with a 1kΩ resolution. It operates in a constant current mode, meaning it aims to induce a set current value through the resistor measured and therefore applies a tunable polarization and measures the drop of polarization over a known resistor (R_{ref} and U_{ref}) and an unknown one (R_{meas} and U_{meas}) (Equation 1).

$$R_{meas} = \frac{U_{meas}}{U_{ref}} \cdot R_{ref}$$ **Equation 1**

DMM Keysight E34972A devices were installed at the other two systems and allowed resistance monitoring of several sensors at once (20 per scanner card with 3 card slots). Typically, up to 4 sensors were investigated and measured simultaneously, as this represents the number of sensor sockets per test chamber. The maximum resistance range of such a device is at 100 MΩ, but was extended by putting a known 100 MΩ resistor in parallel to each measured sensor. This allowed measurements up to around 5 GΩ with sufficient precision. The actual sensor resistance was calculated by Equation 2. Same as the Keithley DMM, this device operates in a constant current mode.

$$R_{sensor} = \frac{R_{meas} \cdot 100M\Omega}{100M\Omega - R_{meas}}$$ **Equation 2**

4.3 Operando DRIFTS setup

The term “operando” should be understood as an experimental technique that is applicable to a functional material in its operation condition. For gas sensitive materials this includes the presence of a gas atmosphere (typically at 1 atm), the possibility to heat the sensor (RT to 400 °C) and to read out its resistance. Effectively, a real sensor device is used, operated and evaluated normally, while an additional technique is utilized to acquire additional material characteristics. In this work, information on the chemical state of the surface was deem the most valuable and therefore infrared spectroscopy was the operando technique of choice. There are other methods available in today’s toolbox, ranging from various spectroscopic methods, over catalytic conversion measurements, to electronic techniques such as AC impedance (EIS) or work function changes (Kelvin probe).

Ex-situ, in-situ, and operando techniques are commonly used to study functional materials by comparing the experimental conditions to those during actual operation. Operando methods – widely used in catalysis research – combine spectroscopic techniques with real-time measurements of a material’s catalytic activity. This approach has been extended to various functional materials, including gas sensors. In operando gas sensor research, the sensor response (for example, the resistance of a SMOX-based sensor) is measured simultaneously with additional properties using spectroscopic or electrical techniques.

Although definitions can vary, a common classification is as follows:

- Ex-situ experiments: Measurements are conducted under conditions (temperature, pressure, atmospheric composition) that do not replicate the sensor's actual operating environment.
- In-situ experiments: Measurements are performed under conditions relevant to gas sensor operation, but the sensor response is not evaluated simultaneously.
- Operando experiments: Measurements are taken on real sensor devices under realistic operating conditions, with simultaneous evaluation of the sensor response.

IR spectroscopy, which is used to study molecular vibrations, can identify molecules or functional groups. A vibrational transition is IR-active only if the dipole moment of the molecule changes during the vibration. The energy of an IR transition depends on factors such as the mass of the vibrating atoms and the strength of the bonds between them. Figure 8 illustrates the potential curve of a diatomic molecule.

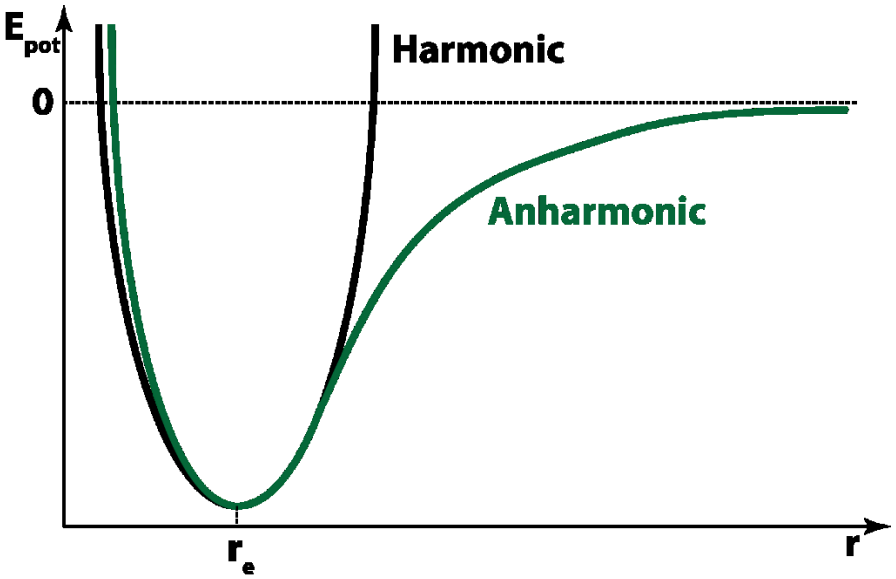

Figure 8: For higher energies the parabolic shape of the harmonic oscillator (black) fails and the potential energy curve of a diatomic molecule is better described by introducing anharmonicity (green). Common approximation models are the Lennard Jones potential and the Morse potential.

Near the equilibrium distance between the two atoms, the potential can be approximated as parabolic, and the vibration behaves like a harmonic oscillator. Based on this model, the wavenumber of the IR transition depends on the masses of the atoms (reduced mass, μ) and the bond strength (force constant, k_f), as described by Equation 3, where c_0 represents the speed of light.

$$\tilde{\nu} = \frac{1}{2\pi c_0}\sqrt{\frac{k_f}{\mu}} \qquad \textbf{Equation 3}$$

According to Equation 3, vibrations involving lighter atoms and/or stronger bonds occur at higher wavenumbers compared to those involving heavier atoms and/or weaker bonds. This bond strength effect can be observed when comparing the O-H stretching vibrations of different surface hydroxyl groups. For instance, the O-H stretch vibration of acidic hydroxyl groups appears at lower wavenumbers; on zeolites, the O-H stretch band of weakly acidic hydroxyls is found around 3745 cm^{-1}, while that of acidic Brønsted sites is around 3610 cm^{-1}. For hydroxyl groups on metal oxide surfaces, the acidity and thus the position of the O-H stretch band depend on the cation coordination of the oxygen atom in the hydroxyl group. On zeolites, the band at 3745 cm^{-1} corresponds to terminal groups on silicon (Si-OH), while the band at 3610 cm^{-1} is attributed to bridged hydroxyl groups (Si-OH-Al). When the proton in a hydroxyl group is replaced by deuteron, the corresponding O-D stretch band appears at a lower wavenumber. The shift can be calculated by:

$$\frac{\tilde{\nu}_{OD}}{\tilde{\nu}_{OH}} = \sqrt{\frac{\mu_{OH}}{\mu_{OD}}} \qquad \textbf{Equation 4}$$

According to Equation 4, the theoretical shift for this substitution is 0.728, which is slightly lower than the experimental value of 0.737 for OH/OD exchange in terminal OH groups on SnO_2. The discrepancy between the experimental and theoretical shifts is due to the limitations of the harmonic oscillator approximation for diatomic molecules, which is not sufficient to describe surface hydroxyl groups as part of more complex structures like surfaces or solids.

Infrared (IR) spectroscopy is a key technique for studying the properties of solid materials. The most common method is transmission spectroscopy, where IR light is passed directly through a sample. For solids, this usually means preparing very thin pellets or diluting the sample in potassium bromide (KBr) to allow sufficient light

to pass through. Transmission measurements have been especially important in in-situ studies of SnO_2-based gas sensing materials, providing valuable insights into their behavior under controlled conditions.

Another powerful approach is diffuse reflectance spectroscopy, which became more accessible with the advent of commercial mirror optics. This method collects IR light that is scattered by the sample rather than transmitted. A specialized form of this technique, known as Diffuse Reflectance Infrared Fourier-Transform Spectroscopy (DRIFTS), offers simpler sample preparation and is particularly well-suited for operando measurements on thick film layers – such as those found in SMOX-based gas sensors – where the material is examined in conditions that mimic its real-world use.

It is also important to note that when IR light interacts with a material's surface, it can be reflected in two ways. Specular reflection is a mirror-like reflection that maintains the direction of the incoming light, whereas diffuse reflection results from multiple scattering events, including reflection, refraction, and diffraction within the material. In practice, most surfaces exhibit a combination of both specular and diffuse reflection, as illustrated in Figure 9.

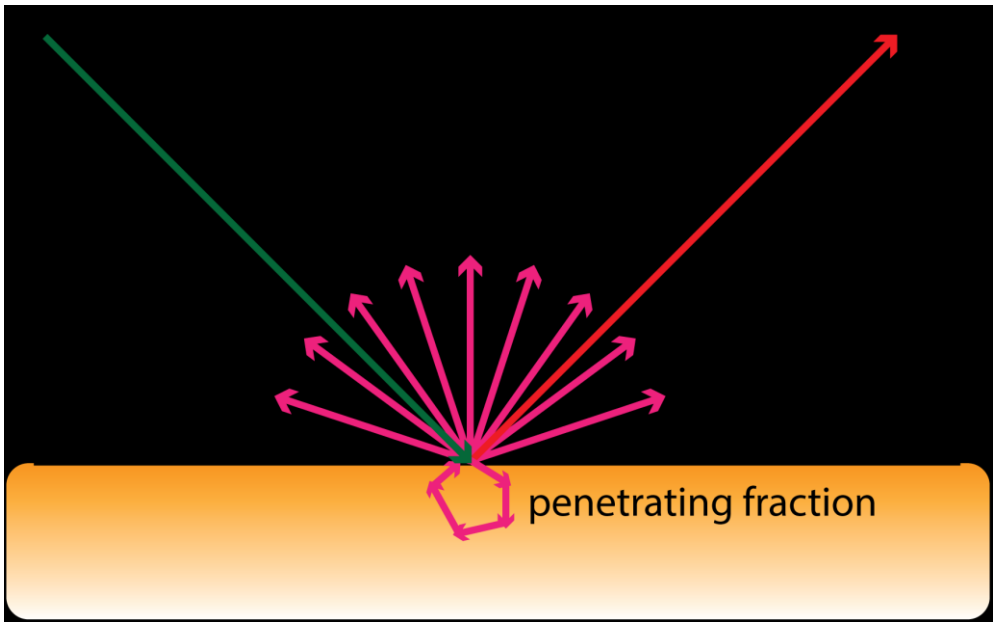

Figure 9: Illustration of reflection processes on a small grained metal oxide surface. The incident beam is reflected as specular and diffuse beams. The diffuse part is captured by the detector and contains spectroscopic information from its interaction with the metal oxide material.

Specular reflection occurs mainly on smooth and polished surfaces, while diffuse reflection dominates on rough and matte surfaces. In samples made up of individual grains smaller than the wavelength of the radiation, diffuse reflection is the dominant process. The radiation penetrating the sample during diffuse reflection can be partially absorbed, providing spectroscopic information about the sample. To record a spectrum using diffuse reflectance, special mirror optics are used to capture as much diffuse reflected radiation as possible. DRIFT spectra display the same qualitative features as transmission spectra, but quantitative analysis requires the Kubelka-Munk theory for diffuse reflectance spectroscopy.

5. Results and discussion

5.1 Characterization of low temperature sensing properties

A first assessment of the gas sensing properties of the three IPC1000 materials in a low and high temperature regime was performed. Two types of substrates were used to manufacture sensors, discriminating themselves by their electrode material. The choice of electrode materials can significantly alter the sensor properties, as interactions between MOX-layers, precious metal surfaces and gas species can induce various electrical and chemical effects. Initial expectations for the utilization of gold electrodes were an acquisition of insights into the "raw" properties of the MOX-layer, due to a reduced catalytic activity towards the target gases H_2 and CO. Platinum electrodes were expected to unlock the full potential of the sensors by increasing the accessibility to reactive gas molecules

5.1.1 DC resistance measurements on Al_2O_3 substrates with gold electrodes

As is turned out the results of the first few measurements using sensors with gold electrodes were very poor, showing hardly any response to hydrogen gas, even at high concentrations. Figure 10 gives an overview of the sensor signals to 1000 ppm hydrogen gas in a background of synthetic air (40% relative humidity).

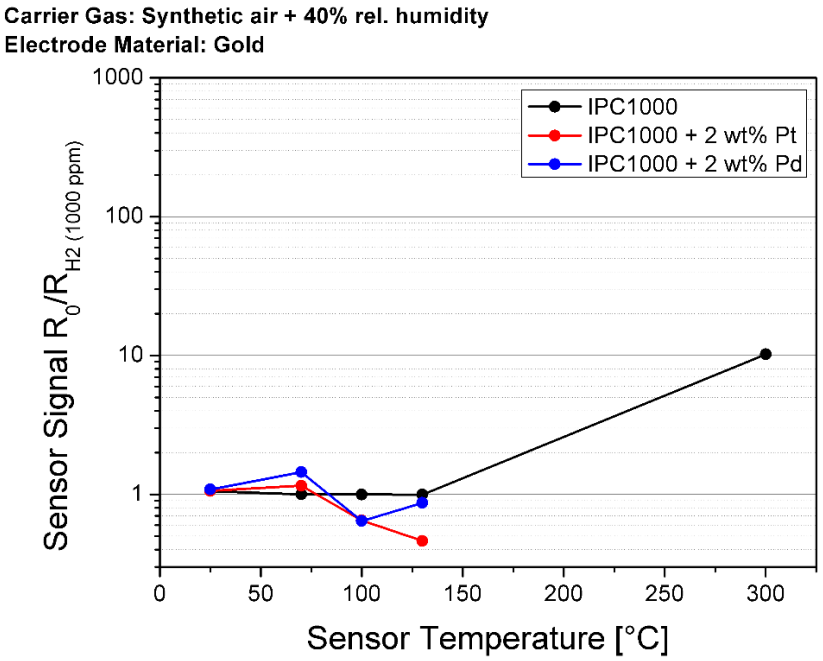

Figure 10: Temperature dependence of the sensor signals for IPC1000 materials on gold electrodes. Test gas was 1000 ppm of H_2 in a synthetic air (40% relative humidity) atmosphere. In the low temperature regime all signals were close to 1 or even below, translating to no response at all or atypical p-type response to a reducing gas.

The three different IPC1000 materials on gold electrodes were operated at room temperature (~25 °C), at 70 °C, at 100 °C and at 130 °C. The undoped IPC1000 sensor was additionally tested at 300 °C to check its general functionality.

In the absence of ample amounts of catalytically active platinum, typically provided by electrode and heater elements if such substrates were used, the sensors were unable to interact properly with hydrogen gas and therefore showed little to no sensor response. At 70 °C the materials containing incorporated dopant metals managed to achieve minor responses, but towards higher temperatures showed atypical behavior by climbing to higher resistances in the presence of a reducing gas. This was unexpected for n-type semiconductor materials and was investigated separately but shall not be further discussed within this work. Due to the absence of any significant sensor response at low temperatures, further investigation of these types of sensors was consequently discontinued and the focus shifted to platinum-type substrates.

5.1.2 DC resistance measurements on Al_2O_3 substrates with platinum electrodes

For the investigation of IPC1000 on platinum coated substrates a different test regime was utilized. The focus was shifted towards room temperature capabilities of the materials towards CO and H_2 as an analyte gas. In order to achieve comparable results, the testing was initialized with one cycle of the test gas sequence at 300 °C, then cooled down to room temperature and followed by continuous repetitions of the test gas sequence.

This allowed for comparisons between hot and cold state sensor performance and the ability to uphold their sensing characteristics over time.

All measurements were performed in humidified air as a carrier gas (50% RH) with a flowrate of 250 sccm. The test gas sequence consisted of three 1 hour pulses of CO with 50, 150 and 500 ppm concentration, then three 1 hour pulses of H_2 with the same concentrations. After a recovery period of 3 hours, the sequence was repeated.

Data was acquired over the course of 10 days and is presented in Figure 11, Figure 12 andFigure 13.

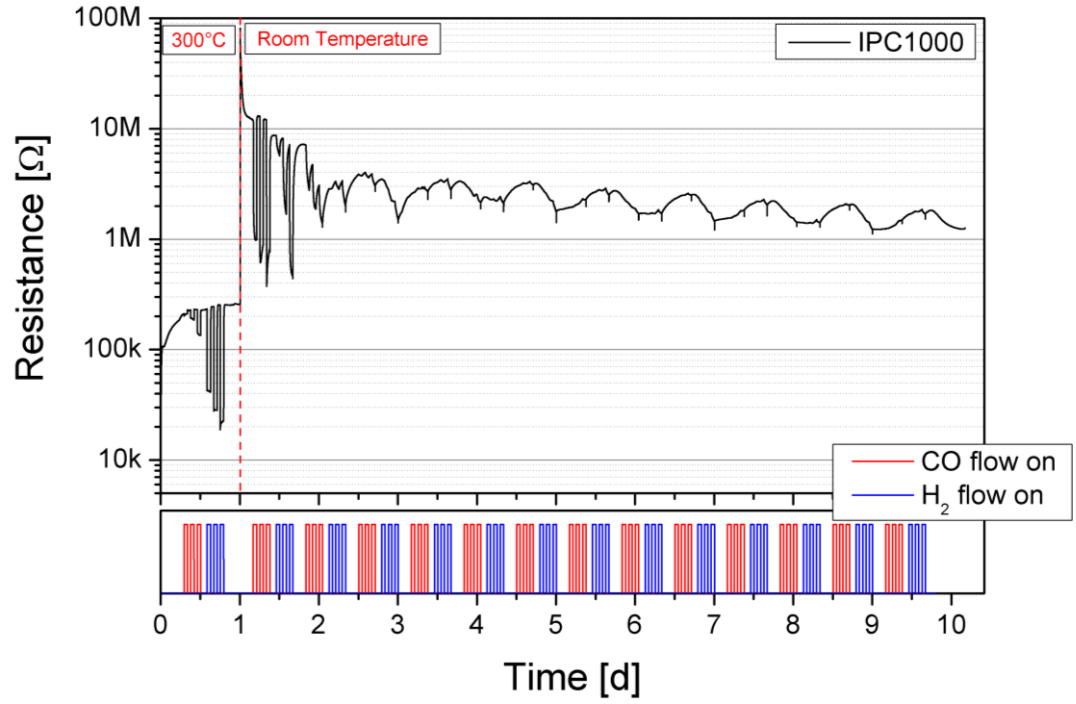

Figure 11: DC resistance measurement of undoped SnO_2 (IPC1000). For the first 24 hours the sensor was operated at 300 °C and exposed to ramps of CO and H_2 (50, 150 and 300 ppm). On subsequent days the heater was off and the gas sequence was repeated continuously.

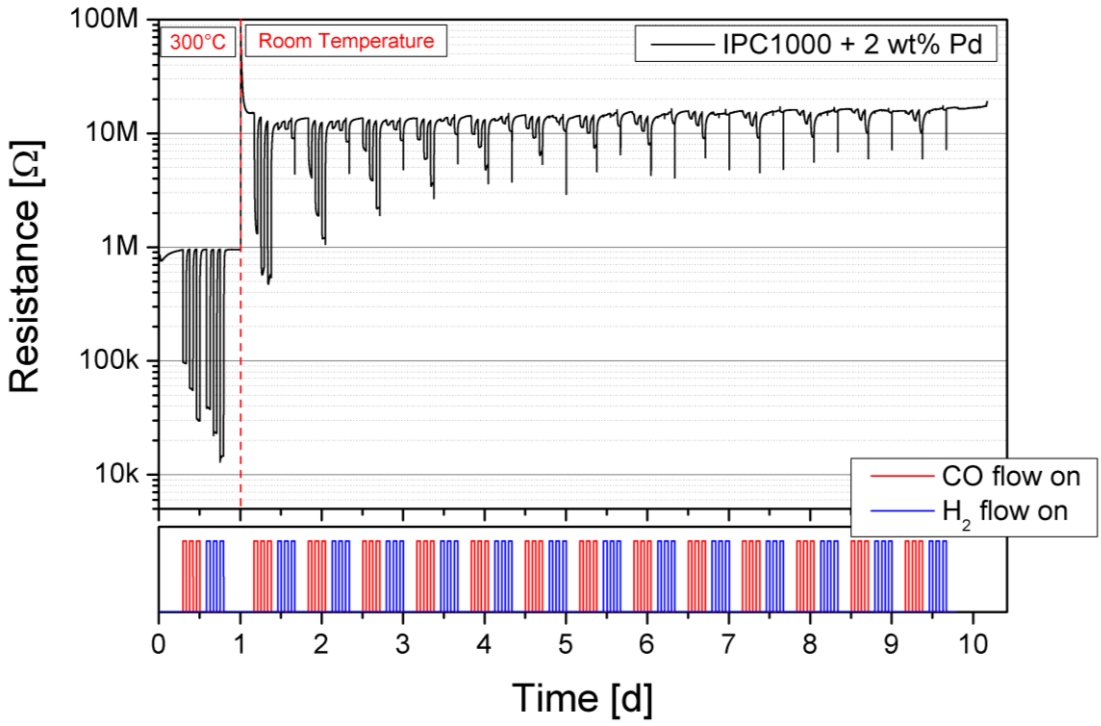

Figure 12: DC resistance measurement of Pd doped SnO_2 (IPC1000 + 2 wt% Pd). For the first 24 hours the sensor was operated at 300 °C and exposed to ramps of CO and H_2 (50, 150 and 300 ppm). On subsequent days the heater was off and the gas sequence was repeated continuously.

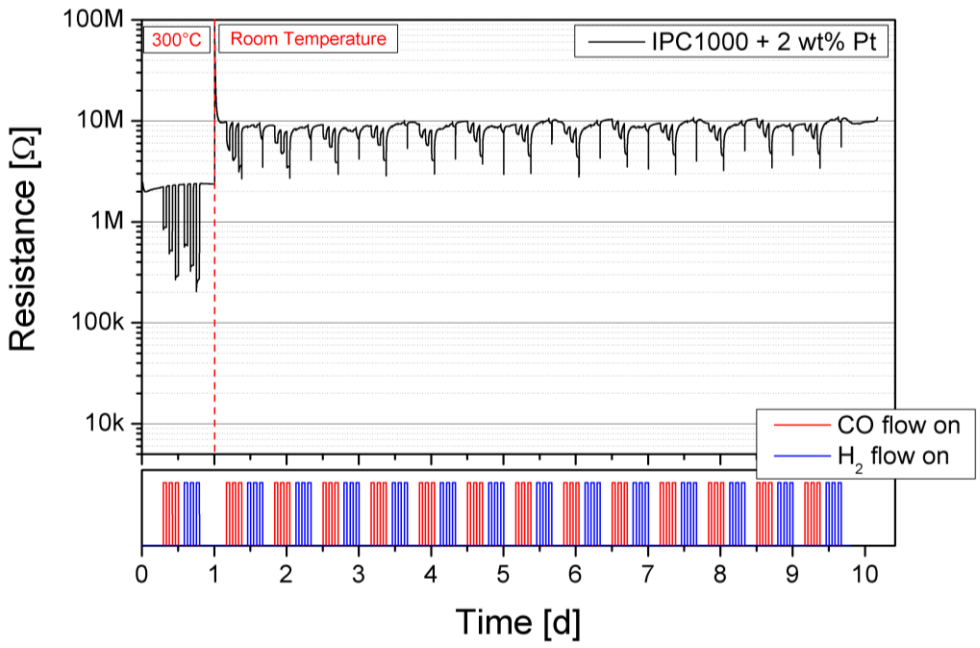

Figure 13: DC resistance measurement of Pt doped SnO_2 (IPC1000 + 2 wt% Pt). For the first 24 hours the sensor was operated at 300 °C and exposed to ramps of CO and H_2 (50, 150 and 300 ppm). On subsequent days the heater was off and the gas sequence was repeated continuously.

The cool down procedure showed an expected increase of resistance for all materials. In the first seconds a sharp overshoot was observed, corresponding to the response any semiconductor would give to a decreased temperature. After a few minutes, resistances settled down to a lower value, though still above the level of 300 °C, as the surface states slowly adapted to the new temperature by altering its concentration of active oxygen species and therefore less trapped charge carriers.

IPC1000 showed unstable baseline resistance over time, with an ongoing resistance drift towards lower values. The doped materials quickly settle for a stable baseline with no noteworthy baseline drift behavior.

Initially, all materials responded well to the presence of CO and H_2, but a decrease over time can be observed at first glance. To evaluate this degeneration of responses over time, the resistance of all 500 ppm CO and H_2 events were extracted, signals calculated and plotted against the corresponding time since cool down. Defined as a sensor signal (S) is the ratio between resistance in clean air (R_0) and the resistance under test gas exposure (R_{gas}).

$$S = \frac{R_0}{R_{gas}}$$ **Equation 5**

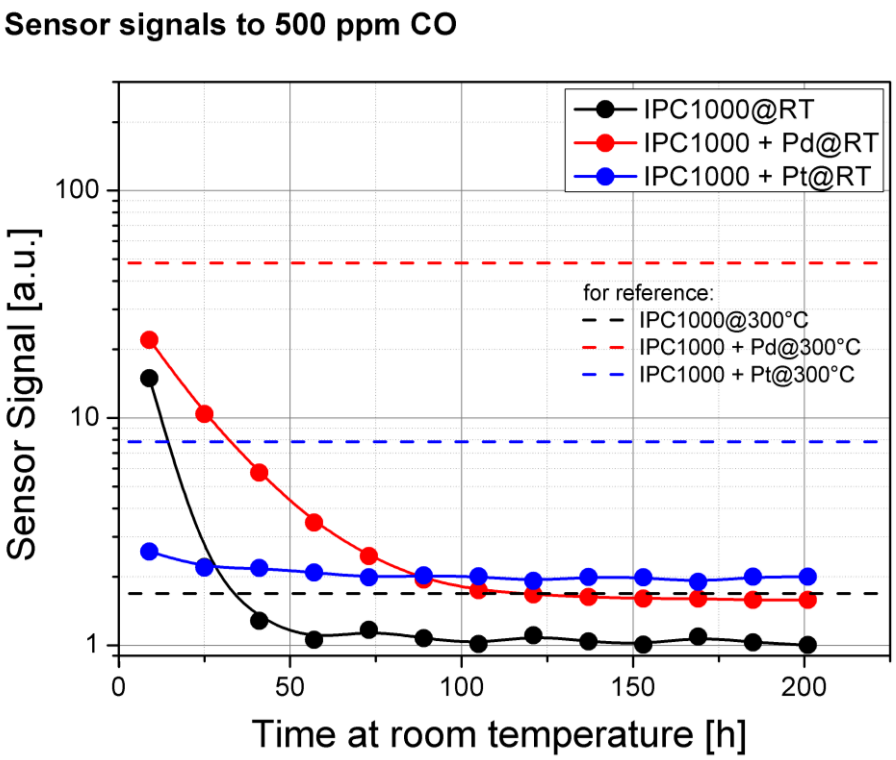

Figure 14: Development of sensor signals to 500 ppm CO over time. Cool down to room temperature occurred at 0 hours in this representation.

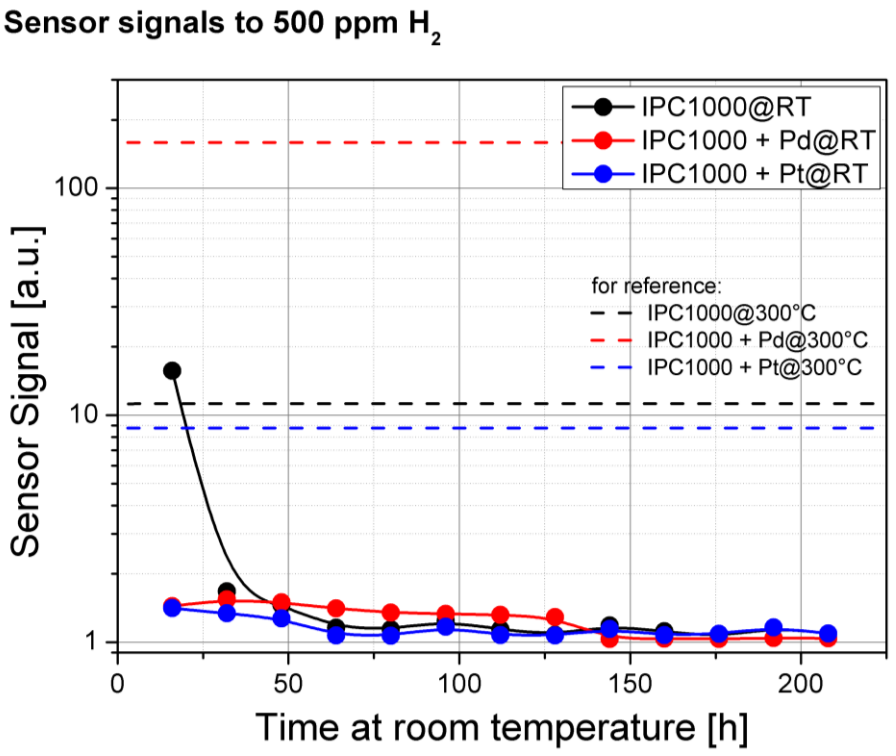

Figure 15: Development of sensor signals to 500 ppm H_2 over time. Cool down to room temperature occurred at 0 hours in this representation.

Figure 14 and Figure 15 illustrate the behavior of the sensors under prolonged RT operation quite well. The undoped IPC1000 had strong initial signals towards both target gases within the first hours after cool down, but also showed the strongest decay. For the second and third repetition of the test cycle, corresponding to roughly 1 to 2 days after cool down, barely any response is left. Additionally, the response time and recovery slowed down significantly and the original baseline resistance could not be retained.

Palladium doped IPC1000 showed the highest initial response to CO, followed by a gradual decrease of performance over the subsequent test cycles. The sensor signals decreased from around 20 down to just shy of 2, but seemed to stabilize at that level. Its initial H_2 performance was poor and continued to decay within the next days to nonexistent.

A different pattern emerged for platinum doped IPC1000 as it missed out on the strong initial performance shown by the other materials, but managed to keep its response to CO very stable over the here tested timeframe of around 200 hours. Similar to IPC1000+Pd it had poor H_2 performance, accompanied by a decaying signal over time.

These results highlight the relevance of temperature history for the evaluation of a room temperature sensor. Performance at room temperature can vary from excellent to poor, just depending on the time passed since cool down. Subsequent chapters will try to give more insight into this phenomenon by surveying the sensors ability to acquire and desorb oxygen, and by conducting spectroscopic studies on the surface species available before and after cool down.

5.1.3 DRIFTS investigation on performance decay over time

A comparable sequence of gas exposures, as in the previous chapter was conducted and in addition to DC resistance data, infrared spectra were recorded in operandi. The initial gas sequence took place at a sensor temperature of 300 °C to identify the involved surface species with the sensor being at a common and proven operation mode. Subsequent the sensor heater was shut off and the gas sequence was repeated several times over the next days while recording spectra of this unheated sensor.

5.1.3.1 Oxygen adsorption/desorption equilibrium at high temperatures

The surface processes of sensing at 300 °C are relatively well understood by now and basically revolve around the equilibrium between surface oxygen and analyte molecules. At elevated temperatures the thermal energy needed to dissociate O_2 molecule is present and existing vacancies can be healed with O^{2-} species. A higher number of ionosorbed oxygen correlates to the formation or an increase of the depletion layer at the surface, resulting in a decrease of conductivity. Even without the presence of additional gas phase reaction partners, an intrinsic equilibrium will form due to temperature dependent desorption of oxygen and partial healing of present vacancies. With the availability of reducing analyte molecules (CO, H_2, etc.) in the gas phase the population of surface oxygen species with be reduced and a new equilibrium of natural desorption, reaction with analytes and re-adsorption will be established.

The process of absorbing oxygen on surface sites S can be described with the following equation:

$$^1/_2\, O_2^{gas} + S \leftrightarrow O_S$$

Adsorbed oxygen introduces acceptor levels which can be ionized via charge transfer from the conduction band to the surface.

$$O_S + 2e^- \leftrightarrow O_S^{2-}$$

On the semiconductor side, this is accompanied by upward band bending (qV_s) resulting in an increase of the Schottky barrier height, effectively decreasing the number of electrons with can reach the surface (n_s). Under the assumption that the Schottky approximation is valid, this can be expressed as

$$n_S = n_B\, exp\left(-\frac{qV_S}{kT}\right)$$

Both terms - the number of ionized bulk donors (n_B) and the exponential function - are temperature dependent.

5.1.3.2 Oxygen adsorption/desorption equilibrium at room temperature

A working hypothesis for the sensing processes of a sensor at room temperature (after a time period of high temperature) would be as follows: Initially the cool down to RT results in a quenching of the current state of the surface as it was established during 300 °C operation, meaning the population of atomic O^{2-} species is still comparably high, but the previous equilibrium of desorption and adsorption of oxygen is disturbed as only molecular oxygen can now fill appearing vacancies. Overall, a decrease of O^{2-} and an increase of O_2^- would be expected. The presence of reducing analyte gas like CO or H_2 should accelerate this population shift and the resulting performance degradation by increased consumption of reactive O^{2-}. Additionally, when remaining for a prolonged time at RT, a number of appearing vacancies are not repopulated with oxygen at all, resulting in a more reduced surface and therefore lower baseline resistance of the layer and possibly a lower response to reducing analytes.

In order to validate or debunk this hypothesis and to acquire a better understanding of surface changes at RT in general, spectra of various gas conditions were reference to one another. Namely, RT baselines over time to 300 °C baseline, RT baselines over time to initial RT baseline, RT baselines to its preceding RT baseline, CO exposure over time to its preceding baseline and H_2 exposure over time to its preceding baseline.

5.1.3.3 DRIFTS results for IPC1000

The first round of experiments was performed on an undoped IPC1000 sensor as the absence of dopant materials should reduce the complexity of data analysis and interpretation. The results for Pd and Pt doped sensors are presented in the subsequent chapters.

Figure 16 depicts the recorded DC resistance data of an IPC1000 and marks the timeslots where infrared spectra were acquired. The gas flow was set to a constant 250 ml/min of humidified synthetic air (50% RH), followed by exposure events of 500 ppm of CO and 500 ppm of H_2 with recovery in between and after.

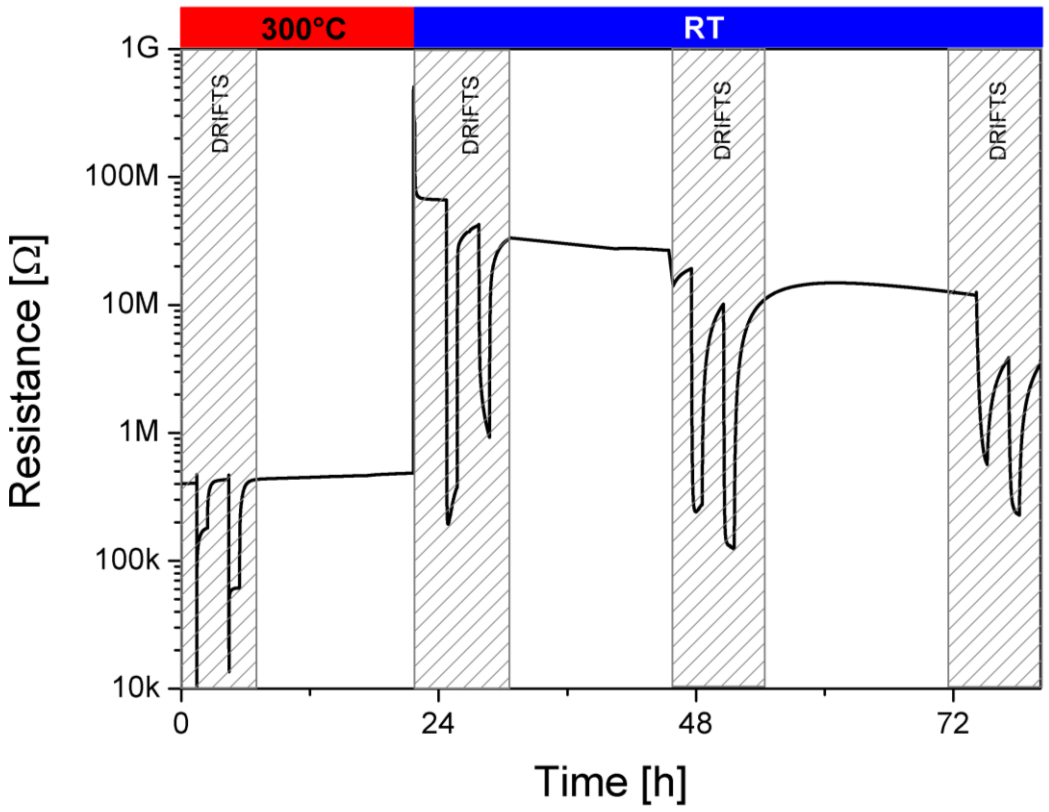

Figure 16: DC resistance data of the IPC1000 sensor, recorded while performing DRIFTS in operando. Shrouded areas mark the timeframe of IR activity. Sensor temperature is labeled on the top side of the graph. Background gas: air with 50% RH. Gas events: 500 ppm CO followed by 500 ppm H_2.

The experiment was design to recreate the results of the initial DC measurement, but now with the added capability of shining IR light on the sample. Indeed, the overall trend was comparable to what was found in Figure 11 and the decaying response to CO and H_2 was captured and the IR spectra analyzed hereinafter.

At first, the focus shall lie on analyzing changes in the surface composition during background gas exposure. The reference spectrum chosen for this analysis was recorded 15 to 30 minutes after turning off the heater voltage. All following baseline spectra were reference to it, and the resulting absorbance spectra can be seen in Figure 17. The very first spectrum - recorded from minute 0 to 15 - was discarded as the cool down process was still ongoing and the temperature therefore undefined.

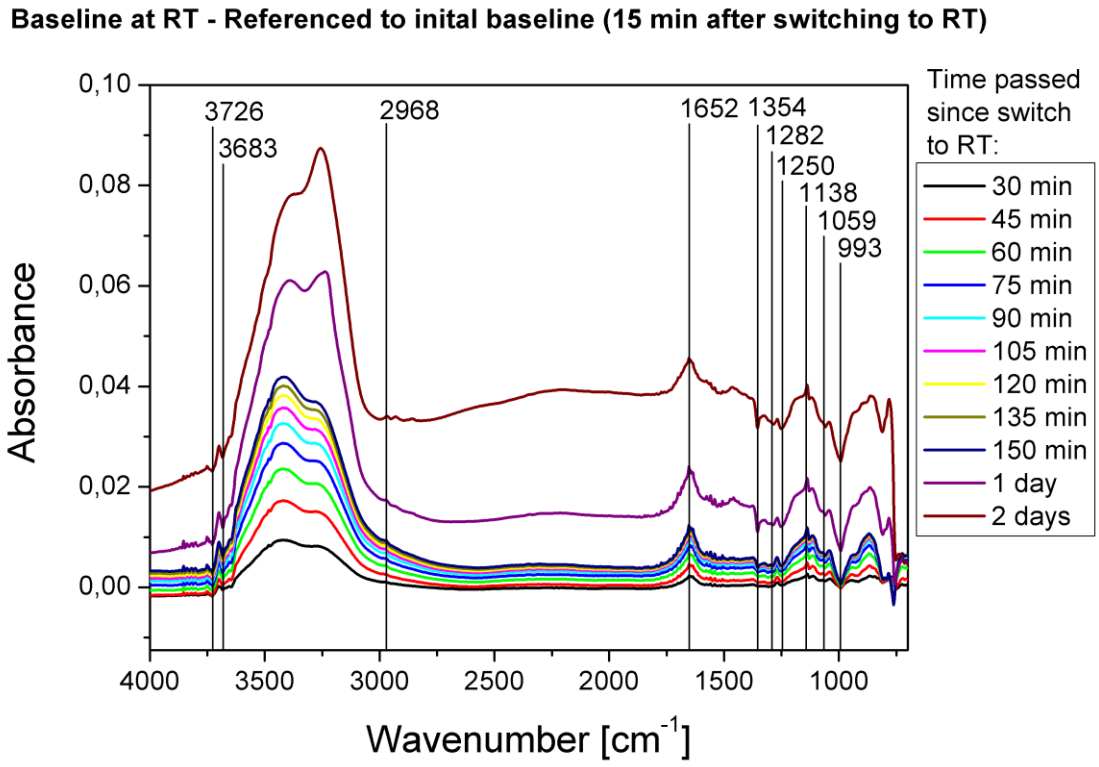

Figure 17: DRIFT spectra of undoped SnO_2 exposed to baseline conditions (air with 50% RH) at room temperature. Each spectrum was recorded at a certain time since cool down as labeled in the legend. The spectrum they were referenced to, was recorded 15 minutes after cool down and had the same baseline gas condition.

At a first glance, the formation of a water layer was apparent as indicated by a broad increase at 1652 cm^{-1} with its surrounding fine structure, representing the bending mode of ligand-bonded molecular water. This also resulted in changes of the hydroxyl group surroundings by interaction with water molecules and subsequent decrease of isolated OH stretch vibrations at 3726 and 3683 cm^{-1}. Furthermore, a decrease of Sn-OH deformation vibrations at 1282, 1250, 1059 and 993 cm^{-1} could be observed, while resulting in a strong increase of interacting OH groups indicated by a broad peak at around 3400 cm^{-1}. These were expected changes occurring due to the increasing presence of interacting water molecules atop the metal oxide surface. Of higher interest was the appearance of a continuously increasing peak at 1138 cm^{-1}. According to Davydov [81] this could correlate to an increased formation of singly ionized molecular oxygen O_2^- and would support the hypothesis of a shift towards this species. Special focus will be put on the behavior of this peak when referencing to different gas conditions. The decreasing peak at 1354 cm^{-1} is generally linked to the reduction of the lattice,

meaning desorption or alteration of bonds of the Sn-O species. This decrease should be expected when interactions with water molecules increase and also when the proposed transfer from atomic oxygen to molecular oxygen takes place, hereby serving as further evidence to the legitimacy of the hypothesis. It is generally accepted that a SnO_2 surface at such low temperatures lacks the ability to split O_2 and thereby heal oxygen vacancies or form mono-atomic oxygen ions, meaning that preexisting oxygen ions will be “lost” over time, either by reaction (e.g. forming –OH), desorption or substitution with molecular oxygen.

The following absorbance bands contain the same RT baseline spectra as before but are this time referenced to the last baseline spectrum at 300 °C (Figure 18). Qualitatively, it should contain similar alterations to the OH environment and its resulting changes in the spectra. On top of that it will contain information directly linked to the differences in temperature. Just by comparing the baseline resistances for RT and 300 °C, a significant difference in free charge carriers is to be expected, which manifests in the reference spectra as lowered absorbance, but the spectra should also reveal changes of surface states, that vanish rapidly during cool down and would not be visible in the previous analysis.

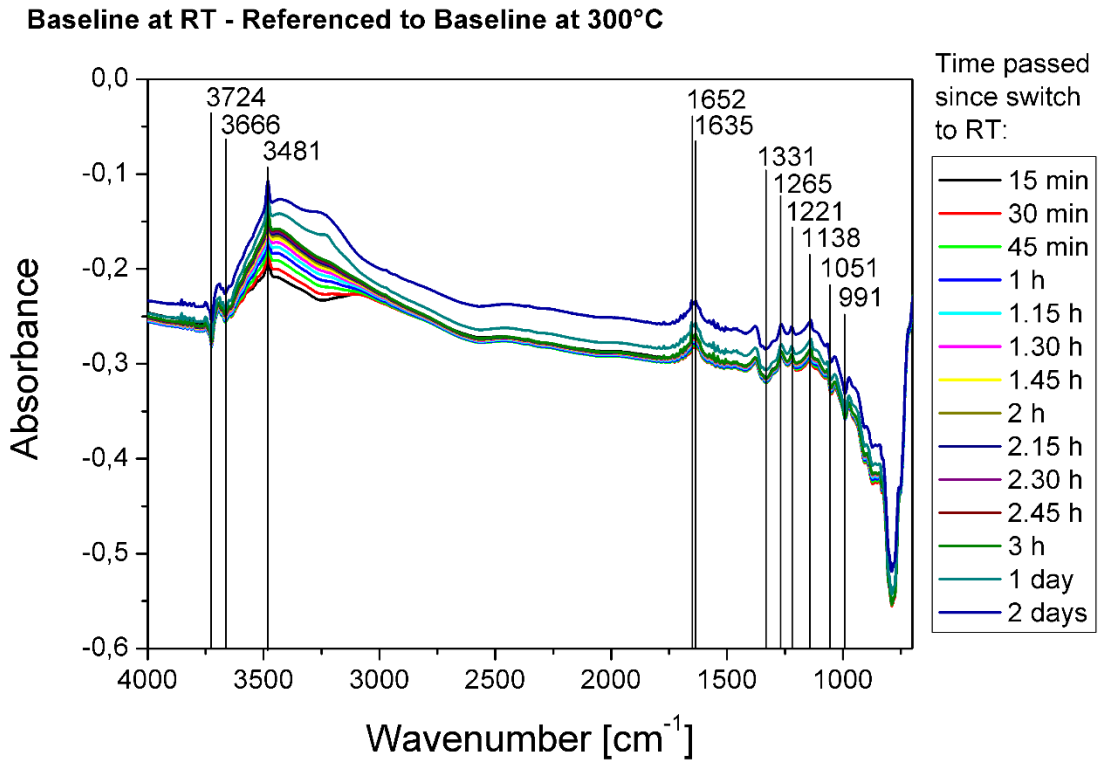

Figure 18: DRIFT spectra of undoped SnO_2 exposed to baseline conditions (air with 50% RH) at room temperature. Each spectrum was recorded at a certain time since cool down as labeled in the legend. The spectrum they were referenced to, was recorded prior to cool down at 300 °C and had the same baseline gas condition.

Concordant with previous results, peaks appear that indicate a build-up of liquid water (1652+1635 cm^{-1}) linked with changes in all OH vibrations (3724, 3666, 3481, 1265, 1051 and 991 cm^{-1}). Again, a peak at 1138 cm^{-1} appears that could indicate an increase of molecular oxygen interacting with the lattice, while reducing or altering the number of Sn-O bonds at 1331 cm^{-1}. A new peak arises at 3481 cm^{-1}, sitting atop the broad signal for interacting OH groups. It represents the increased formation of a different kind of rooted OH groups, less present at 300 °C. Sharp peaks like these, stem from stretching vibrations of non-interacting OH groups – terminal ones for 3724+3666 cm^{-1} and rooted ones for 3481 cm^{-1}. This perturbation of OH groups and observed shift to rooted groups must be a remarkably fast process, as it only appears when referencing a RT spectrum to a 300 °C spectrum. In the previously shown RT to RT spectra no further formation of rooted OH can be found, if any they decrease as surface hydroxylation advances over the course of time.

Another way to look at changes of the baseline after switching to RT can be achieved by referencing each spectrum to the previous one, instead of referencing always to the very first one (Figure 19). This reveals which processes are progressing over time and which ones equilibrate early on.

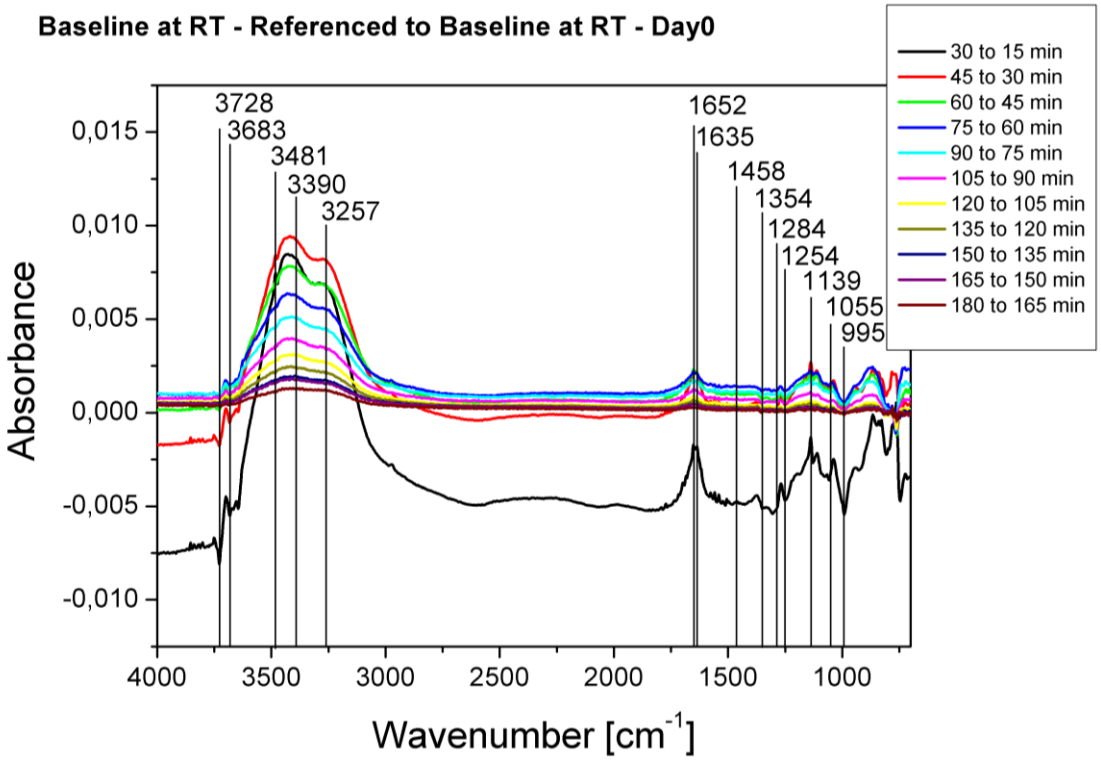

Figure 19: DRIFT spectra of undoped SnO_2 exposed to baseline conditions (air with 50% RH) at room temperature. Each spectrum was recorded at a certain time since cool down and referenced to its previous spectrum.

The signals are clearly the strongest right after switching to RT. The black line represents a referencing of the 2nd recorded spectrum to the 1st, meaning it reflects the surface changes happening within minute 15 to 30 after cooldown, to minute 0 to 15. Most dominant are the peaks for molecularly adsorbed water (1652 + 1635 cm^{-1}) and the resulting interaction with preexisting OH groups (increase of 3400 cm^{-1}, decrease of 3728 cm^{-1}). It is the only referenced sprectrum that shows a clear reduction of the surface in 1284 cm^{-1}, indicating the desorption of O^{2-} as a rather fast process, arriving at a near equilibrium state within the first 30 minutes after cool down. The build up of O_2^- on the other hand can be observed also in later reference spectra, identifying it as a slower process which remains active for at least 2.5 hours before the time window of 15 minutes becomes too short to oberve any meaningful change.

After focusing so far on the baseline changes associated with switching from high to low temperature and their evolution over time, the next paragraph concerns itself with effects introduced by the presence of 500 ppm CO or H_2 gas. It aims to reveal potential differences between involved sensing reactions of both temperature regimes and to allow insights into probable causes of the declining sensor response over a prolonged period at low temperature.

For this analysis, spectra recorded during test gas exposure were referenced to their preceding baseline spectra. The red sprectrum shows the situation at 300 °C, whereas the black spectrum represent the CO event occuring just a few hours after switching to RT. Spectra in dark blue and light blue represent test gas events after 1 or 2 days at RT, respectivley.

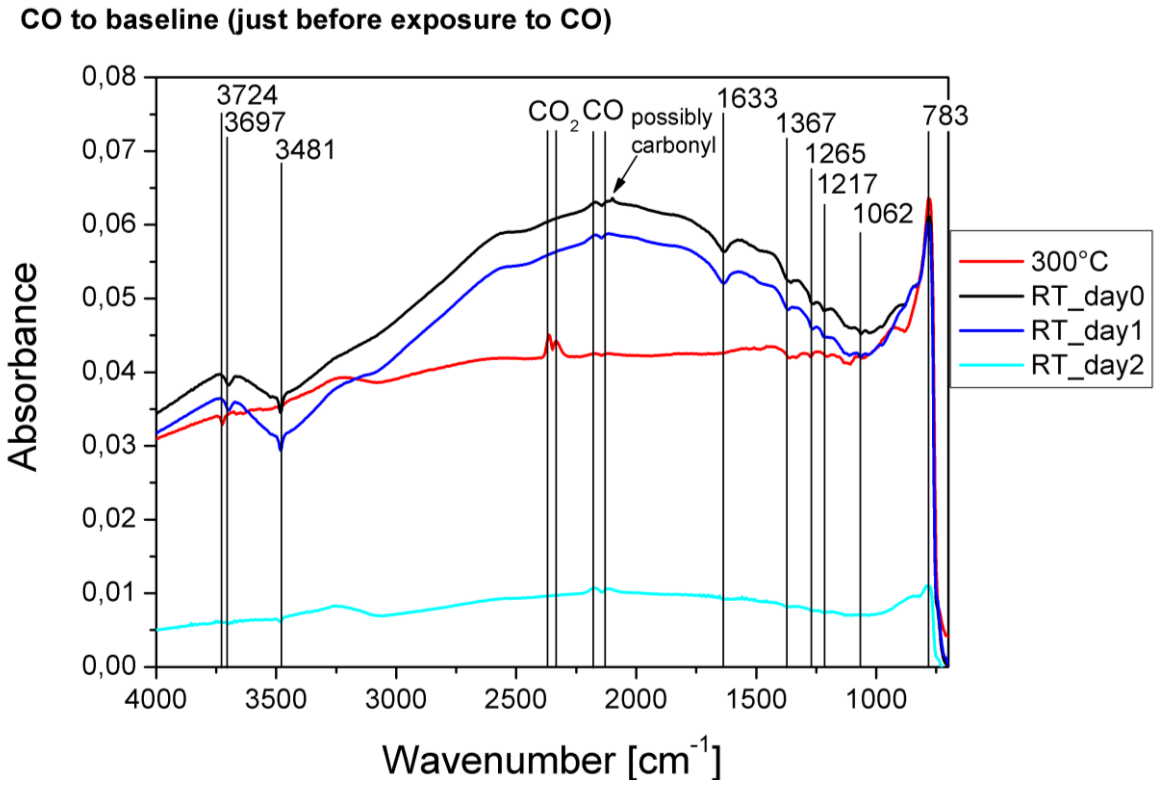

Figure 20: DRIFT spectra of undoped SnO_2 exposed to 500 ppm of CO (in 50% RH). Drawn in red is the spectrum at 300 °C. The black curve was recorded at RT just after cooldown. The blue curves show a CO exposure a full day after cooldown (dark blue) and two days after cooldown (light blue). All spectra were referenced to their respective baseline just before CO exposure.

DRIFT spectra of CO exposure in humid condition at 300 °C have been recorded and analyzed extensively in the past and especially reactions of CO with pristine SnO_2 surfaces are thorougly investigated [19]. The recorded 300 °C sprectrum shows a decreasing band in the hydroxyl region of 3724 cm^{-1}, formation of gas

phase CO_2 at 2363+2333 cm^{-1} and Sn-O lattice overtones at 1367 cm^{-1} and below. Degler et al proposed that the decrease of hydroxyl groups can be explained by the removal of surface oxygen (through the reaction with CO) and a subsequent equilibirium shift towards water vapor and oxygen as presented in the following reaction:

$$H_2O_{gas} + O^{\alpha-} \leftrightarrow 2OH_{ads} + \alpha e^-$$

CO exposure at room temperature significantly differs from exposure at 300 °C especially it terms of hydroxyl group and water involvement. There are now two bands, signaling isolated OH groups, decreased in the presence of CO. These bands are at 3697 and 3481 cm^{-1}, while the latter spikes atop a decreasing broad band representing interacting OH groups. Additionally the amount of molecular water itself appears reduced, as can be seen in 1633 cm^{-1}. As there are no increasing OH bands present anywhere in the sprectrum, the presence of CO seems to stimulate desorption of water related species. The changes in Sn-O lattice overtones remain active for recently cooled SnO_2 surfaces, as can be seen in the bands of 1367 cm^{-1} and below. That means even at RT, CO molecules still find reactive oxygen atoms and subsequently propagate a decrease of hydroxyl groups. Reoxidation and rehydroxylation in turn is signficantly slowed down at RT, causing an equilibirium shift to a more reduced, but also less hydroxylated surface. The absence of gas phase CO_2 bands is puzzeling, as also no other carbon related species like carbonates, carboxylates or formates can be identified. The only clearly identifiable carbon compound is the dosed CO gas. One peculiarity can be seen for the first measurement where a signal appeared in the carbonly region, but this completely vanished for the second and third measurement. It might be a Sn carbonly, but could as well be a Pt carbonly which are reported to appear around 2100 cm^{-1} [82].

A slow or even an absence of desoption of generated carbon species at room temperature is surely in the realm of possibility, but no spectroscopic evidence for the presence of such species can be observed. Other publications have suggested the reaction of adsorbed CO with OH groups at interfacing metal sites, resulting in the formation of formates. This would fit the demonstratable decrease of hydroxyl species and Sn-O lattice overtones, but cannot ultimatly be proven without a correlating appearance of Sn-formate signals.

The sensor response to CO is significantly decreased after 2 days at RT and this is reflected in the IR spectrum. Qualitatively the same bands seem to be present, but at a much less pronounced state. With increasing transformation of active oxygen sites to O_2^- the sensor response continues to decrease. The band at 1139 cm^{-1}, associated with O_2^-, is not affected at all while reacting with CO, which supports the notion of this species as being unreactive and as a blockade to formerly reactive sites.

Spectra of H_2 exposure events were evaluated correspondingly and are shown in Figure 21. Besides a spectrum at 300 °C, several room temperature spectra where recorded over the course of 3 days.

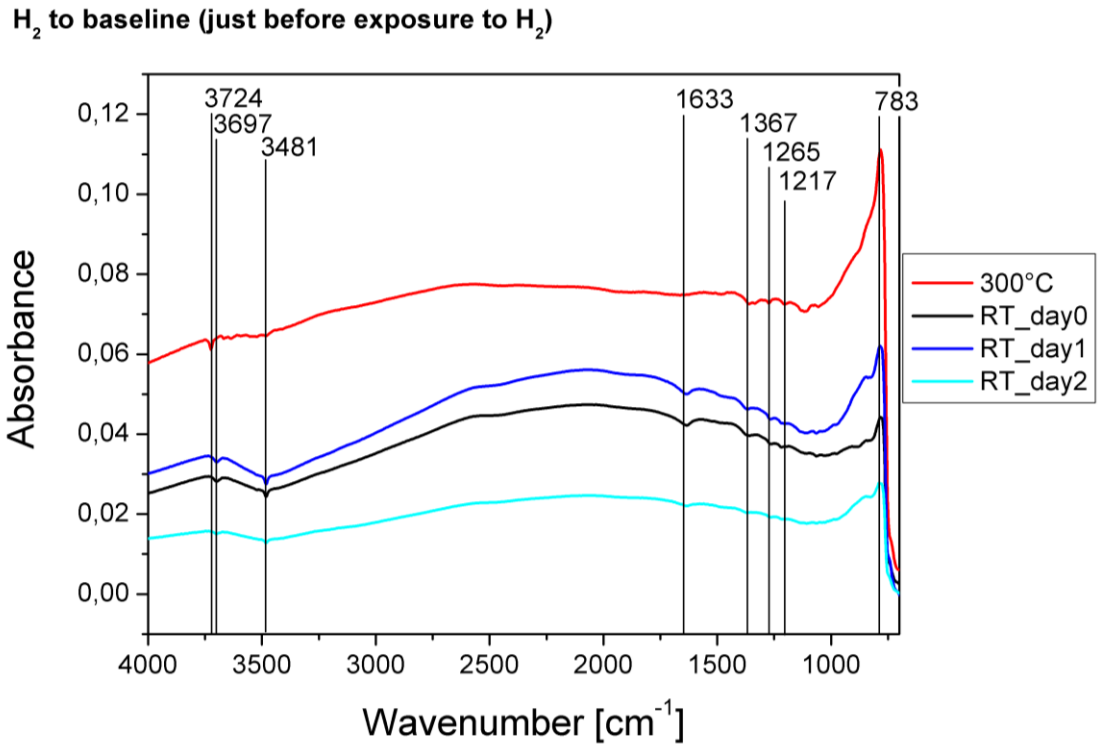

Figure 21: DRIFT spectra of undoped SnO_2 exposed to 500 ppm of H_2 (in 50% RH). Drawn in red is the spectrum at 300 °C. The black curve was recorded at RT just after cooldown. The blue curves show a H_2 exposure a full day after cooldown (dark blue) and two days after cooldown (light blue). All spectra were referenced to their respective baseline just before H_2 exposure.

Besides the obvious lack of CO and CO_2 gas signals, the spectra are very much in line with previously seen changes, indicating comparable reactions taking place and involving the same reaction partners of the metal oxide surface. Isolated hydroxide species and surface bound water molecules are decreased in the presence of H_2 (3724, 3481 and 1633 cm^{-1}), while some degree of surface

reduction takes place (1367 cm^{-1}). After 2 days at room temperature, the once reactive surface sites are seemingly less abundant and in agreement with the lower sensor response, the spectrum loses its characteristic features.

5.1.3.4 DRIFTS results for doped IPC1000

In addition to investigations on a pristine SnO_2 surface, two heavily doped materials were prepared and analyzed in an analogue manner. IPC1000 was decorated with precious metals via powder impregnation, known to form larger agglomerates at the surface of the matrix grains. The resulting powder samples were denoted IPC1000 + 2wt% Pd and IPC1000 + 2 wt% Pt. The chosen precious metals represent well established materials in the SMOX gas sensor world, selected for their enhancing properties regarding stability and sensitivity of resulting gas sensors.

As the results will show, the amount of dopant is generally not enough to produce noteworthy DRIFTS signals attributable to palladium or platinum directly, but will instead alter signals stemming from the underlying SnO_2 lattice and its surface species.

Concerning electrical results for the two materials, a clear increase of baseline stability at room temperature was observed. Palladium doping specifically increased selectivity to CO, with only minor response to H_2, while showing drastically increased recovery speed (Figure 22). CO signals remained relatively stable over the measurement time. Platinum doping showed similar improvements regarding baseline stability, while retaining its H_2 sensitivity and stability over time (Figure 23).

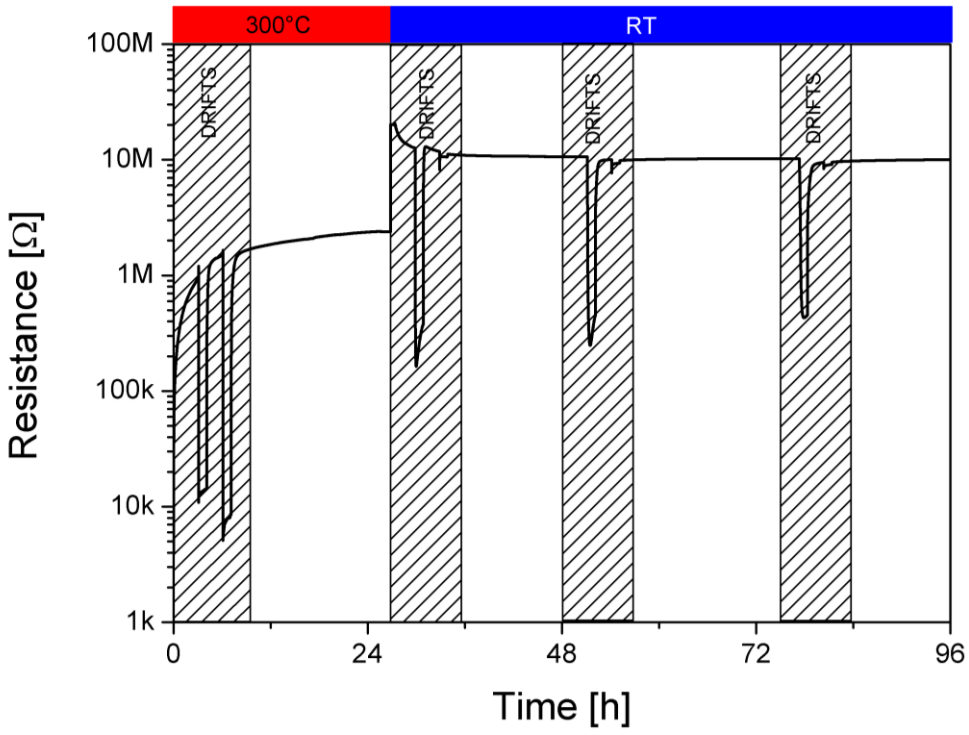

Figure 22: DC resistance data of the IPC1000 doped with Pd sensor, recorded while performing DRIFTS in operando. Shrouded areas mark the timeframe of IR activity. Sensor temperature is labeled on the top side of the graph. Background gas: air with 50% RH. Gas events: 500 ppm CO followed by 500 ppm H_2.

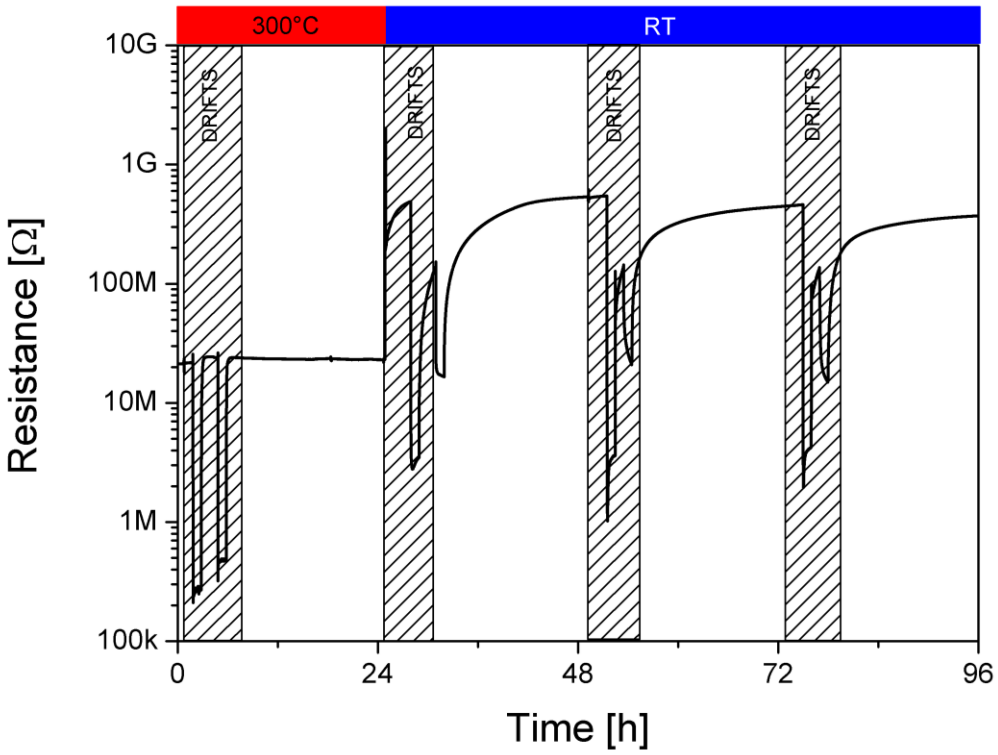

Figure 23: DC resistance data of the IPC1000 doped with Pt sensor, recorded while performing DRIFTS in operando. Shrouded areas mark the timeframe of IR activity. Sensor temperature is labeled on the top side of the graph. Background gas: air with 50% RH. Gas events: 500 ppm CO followed by 500 ppm H_2.

Baseline spectra

In order to allow for direct comparison of undoped, Pd doped and Pt doped results, acquired at the same temperature and gas scenario, all spectra were aligned vertically. The two following figures highlight the changes occurring upon switching from 300 °C to room temperature (spectra recorded 15-30 minutes after cool down) and the changes occurring upon prolonged time at RT (2 days) compared to the very first spectra at RT (0-15 minutes). Shown is the high wavenumber section which contains information about the hydroxyl group situation after cool down.

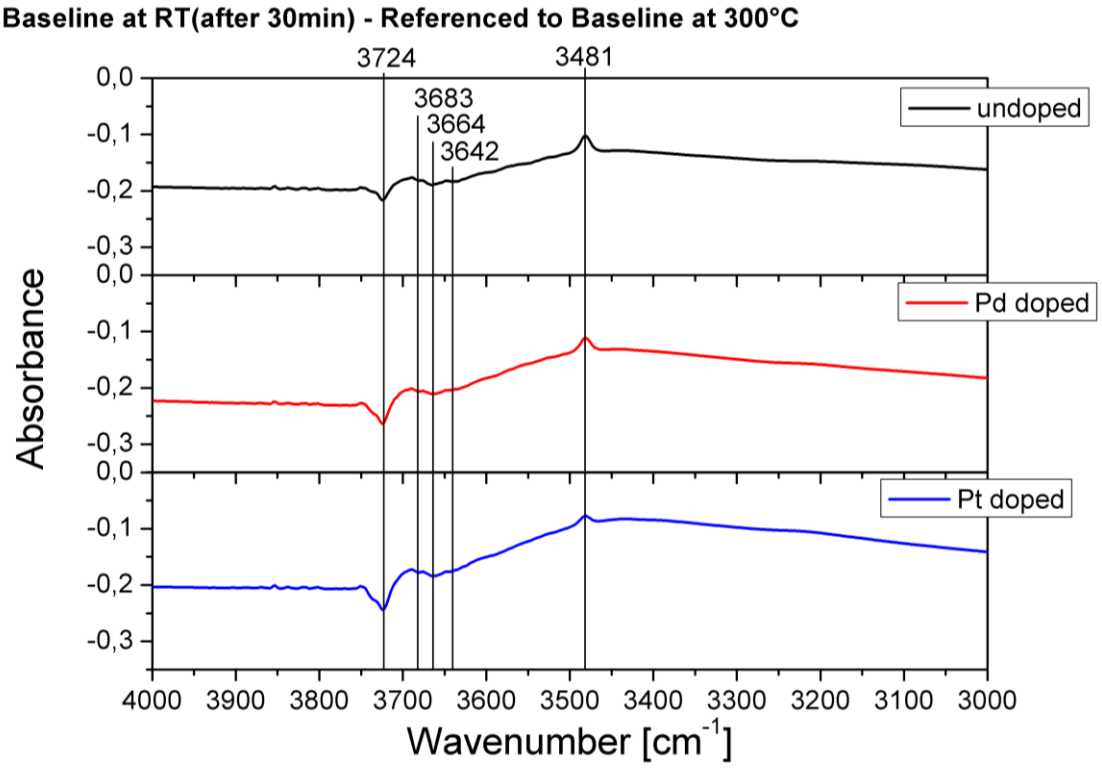

Figure 24: DRIFT spectra of doped and undoped SnO_2 exposed to baseline conditions (air with 50% RH) at room temperature. The spectra were recorded 15-30 minutes after cooldown and referenced to baseline gas conditions at 300 °C. View is zoomed on the hydroxyl region of 3000 cm^{-1} and above.

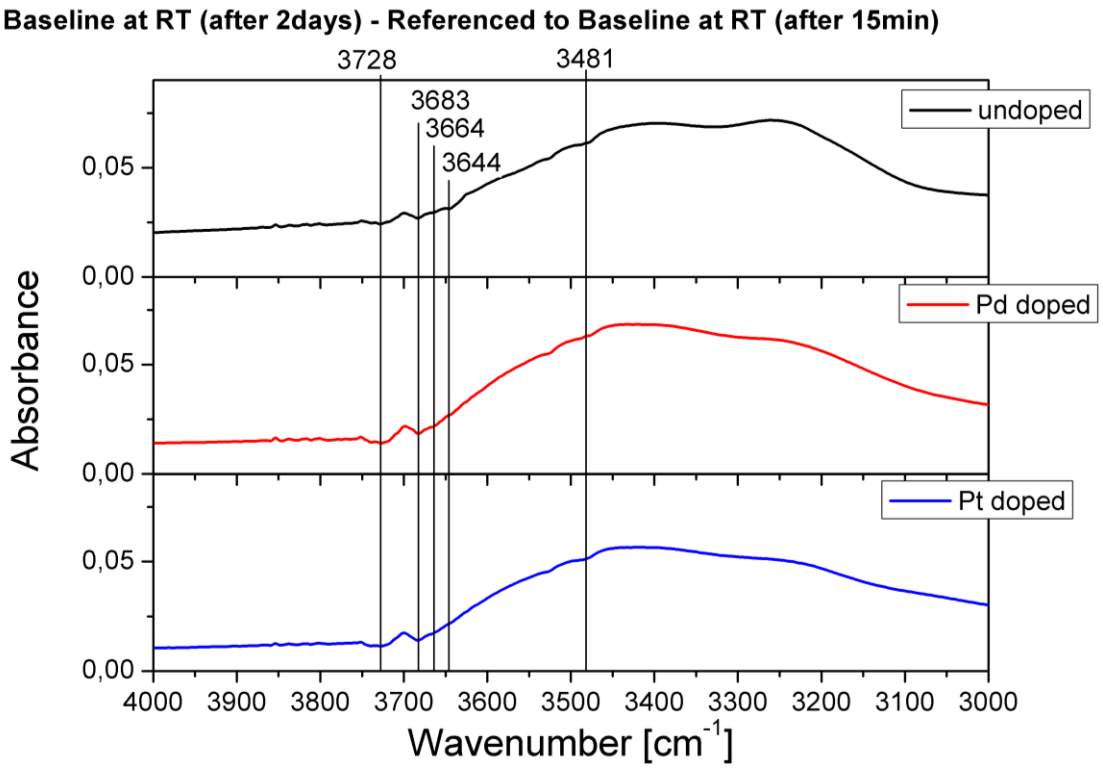

Figure 25: DRIFT spectra of doped and undoped SnO_2 exposed to baseline conditions (air with 50% RH) at room temperature. The spectra were recorded 2 days after cooldown and referenced to baseline gas conditions at RT right after cooldown. View is zoomed on the hydroxyl region of 3000 cm^{-1} and above.

Quite obviously doping had no eminent effect on how the cool down changed the interaction of the regarding surface with water molecules or subsequent changes in hydroxyl groups. Figure 24 shows that immediately after cool down physisorbed water interacted with preexisting OH groups as indicated by the very wide band appearing at 3700 cm^{-1} to beyond 3000 cm^{-1}. In turn stretching vibrations of terminal OH groups were reduced (3724, 3683, 3664 and 3642 cm^{-1}) while a sharp peak at 3481 cm^{-1} appeared. According to the position of this peak it represents an increase of rooted OH groups.

Turning now to the long-term effects room temperature had on the hydroxyl group situation, Figure 25 revealed a continued increase of interacting groups, while isolated (terminal) groups declined further. The initially formed rooted OH groups were hardly affected by prolonged RT conditions. If any, they slightly diminished again after 2 days.

As stated in the previous chapter, the physisorption of water has both a quick onset and a continuous increase over time. The resulting relative increase of interacting

groups and decrease of terminal groups can easily be followed, whereas the relative increase of rooted OH groups wouldn't necessarily be expected. Possibly the location of rooted groups, sitting "deeper" in the lattice, shields them to some extend from interacting with surface bound water molecules and the stretching vibration of the species remains largely unchanged. Doping of the material appears to have no direct effect on any of the mentioned water related changes.

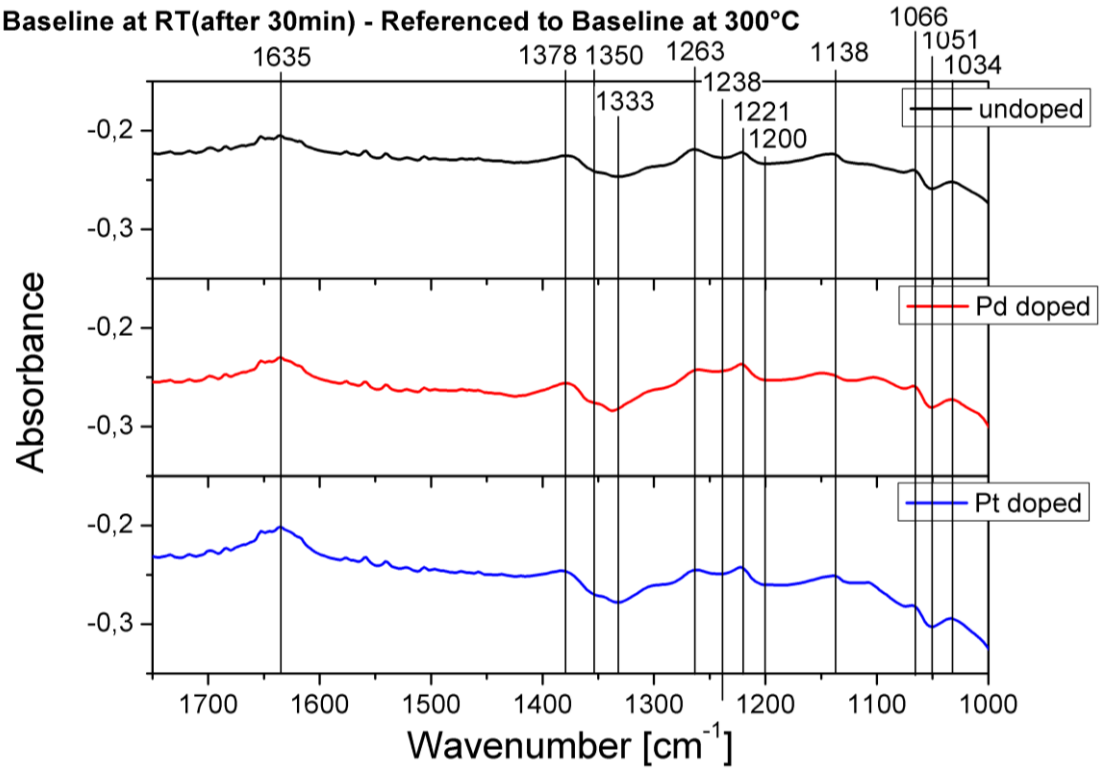

Figure 26: DRIFT spectra of doped and undoped SnO_2 exposed to baseline conditions (air with 50% RH) at room temperature. The spectra were recorded 15-30 minutes after cooldown and referenced to baseline gas conditions at 300 °C. View is zoomed on the oxide region of 1000 cm^{-1} and above.

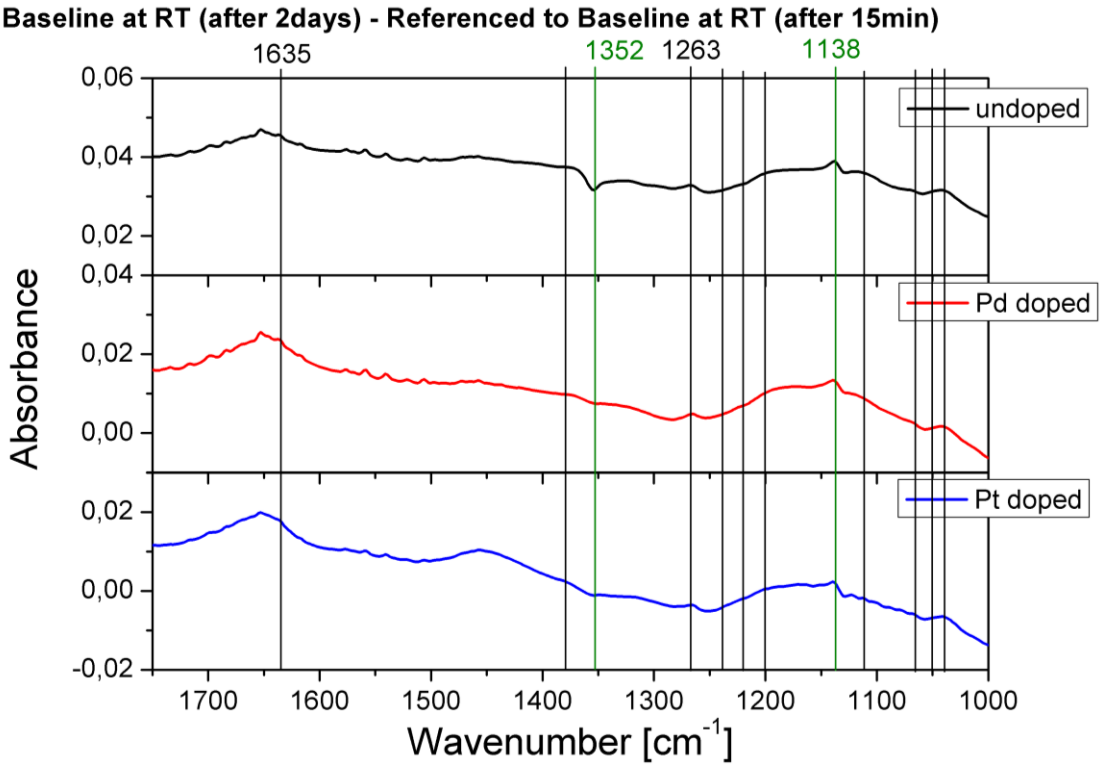

Figure 27: DRIFT spectra of doped and undoped SnO_2 exposed to baseline conditions (air with 50% RH) at room temperature. The spectra were recorded 2 days after cooldown and referenced to baseline gas conditions at RT right after cooldown. View is zoomed on the oxide region of 1000 cm^{-1} and above.

5.1.3.5 Interpretation/Summarization of DRIFT results

The goal of this investigation was to better understand the processes occurring on a SnO_2 surface right after it has been cooled down to room temperature and its subsequent transformation over time, causing the electronic signals to drift to lower resistances and reduced signals to test gas exposure.

The data presented in Figure 19 suggests that just minutes after cool down major changes in regards to hydroxylation takes place and the accumulation of molecular water can be seen. Already present hydroxyl groups undergo a transformation from being previously sparse and isolated to now experiencing the presence of neighboring hydroxyl groups and water molecules, causing their infrared to shift to lower wavenumbers and strong signals appearing at around 3400 cm^{-1}. Although most pronounce right after cool down, this process apparently continues on over time leading to an increasingly hydroxylated surface.

When turning to the effect the cool down has on oxygen adsorption and its respective ionized forms, the peak at 1139 cm^{-1} could indicate an increase of molecular oxygen ions while simultaneously observing a reduction of the material,

probably caused by the presence of water and the inability to recreate atomic oxygen ions anymore.

5.2 Performance screening at low temperatures

In order to systematically identify the magnitude of a repeatable and stable performance towards a selected target gas at low temperatures, the following experimental procedure was conceived. A gas mixing system supplied a constant flow of either dry synthetic air or humidified synthetic air (40% r. h.) to a sensor chamber. The sensors within were initially heated to 400 °C for 2 hours and then cooled down to 30, 70, 130 or 300 °C for 24 hours, still in the respective background gas. For the next 12 hours H_2 was mixed into the gas stream at a concentration of 500 ppm. Finally, H_2 was removed again from the flow and recovery at baseline conditions was monitored for another 24 hours. These long timings were chosen to enable sensor responses to approach equilibrium and to allow for properly drawn conclusions. The initial heat-out removes the variability that a different temperature history would add to the sensor behavior, by having a well-defined and periodic high temperature sequence. An exemplary plot for one such experiment is given in Figure 28 (recovery not shown in full).

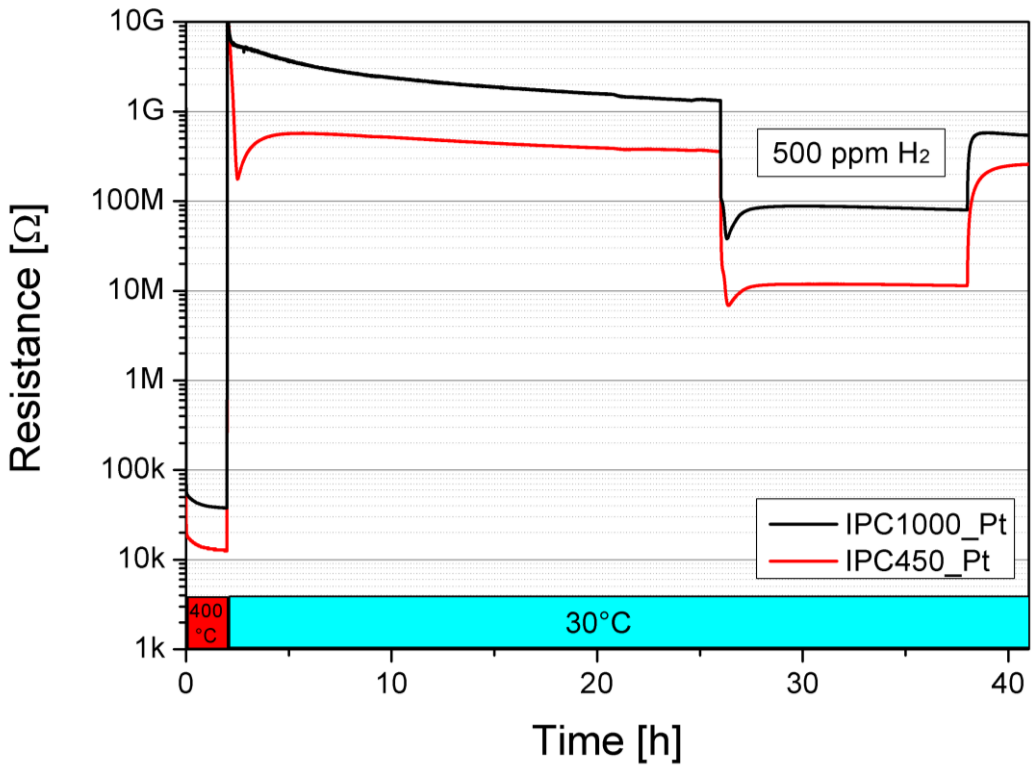

Figure 28: DC resistance measurement aimed to establish equilibrated sensor responses at varying sensor temperatures. A 2-hour heating pulse of 400 °C precedes each measurement to ensure a defined temperature history.

To cover all materials and conditions a total of 30 experiments were run and sensor signals were calculated by taking the ratio between baseline resistance and the resistance under H_2 exposure. The summarized results are shown in Figure 29.

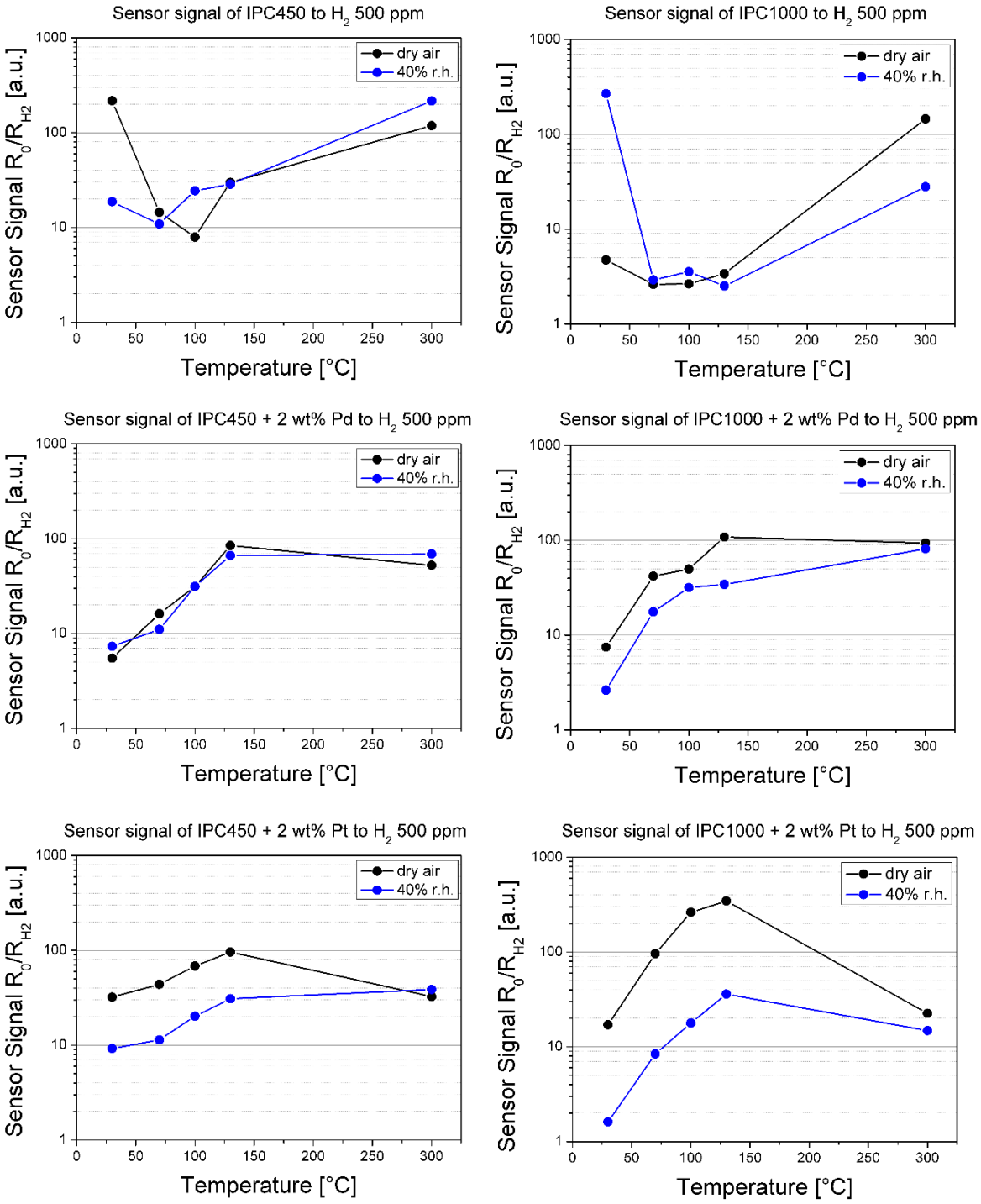

Figure 29: Temperature dependence of the signals to 500 ppm H_2 in dry and humid air.

Qualitatively the undoped materials IPC450 and IPC1000 were quite distinct from their doped variants. Both undoped variants went through a minimum at intermediate temperatures and reached their highest sensor signals at RT and 300°C. In humid conditions most materials suffered from lower signals towards H_2,

with some notable exceptions. Undoped IPC1000 at RT had exceptionally high signals in humid conditions, not seen by any other material. Pd doped IPC450 on the other hand had near humidity independence and showed, like all doped variants, maximum signals at 130 °C. In contrast, the undoped variants peaked at 300 °C.

In light of the insights gained from DRIFTS investigations, the allotted 24 hours after cool-down may have already had a negative effect on the signal strength, but within themselves, the results were very comparable. They showed that a strong H_2 response generally required elevated temperatures. An exception to this trend could be seen for the undoped variants, as they showed surprisingly high signals at RT, declining at 70 °C, but then rising again with higher temperatures.

5.3 Temperature modulation investigations

The majority of commercially available SMOX sensors are designed to be operated at a high and constant temperature, typically 300 or 350 °C. In fact, they work more stable after a prolonged time at operation temperature and shutting them off regularly can disturb baseline stability and gas response reproducibility. There are now some products available, that employ a periodical on/off cycle with fixed timings for heat pulse and resistance read out during that pulse, but the main motivation for doing so is reduced energy consumption, not operation at room temperature. Examples for this type of operation are Sensirion's SGP40 (in low power mode) or Figaro's TGS8410. Very few models come to mind, where the heating pulse is utilized to condition (or oxidize) the sensing layer prior to measuring the resistance at RT. Figaro's TGS2442 sensor uses this method to achieve significant CO selectivity, while maintaining stable baseline and gas response.

Another approach, not yet realized in commercial SMOX sensors, would entail a more complex temperature profile for additional discriminatory capabilities and potentially other benefits to gas sensing properties. Drawbacks to this approach are increased complexity of evaluation algorithms, demand for higher development efforts and lower sampling frequency.

Results of the previous chapter confirm that here tested materials appear to be quite capable sensors at RT, provided they get reconditioned regularly by applying a high temperature state. IPC450 with 2 wt.% Pt was selected as the best

performing material over a wide temperature range and subjected to temperature modulation experiments.

Timing and temperature step sequence had to be defined and it was decided for a temperature staircase, ramping up and back down, with 1 hour hold time at each step. The temperatures covered 25 to 400 °C. With a cycle length of 17 hours, this operation mode was more of scientific nature, than application targeted. It aimed to acquire steady state resistances at each temperature in order to provide reproduceable results. Each gas condition was kept constant for two runs of the temperature cycle and the second cycle was plotted for comparison in Figure 30.

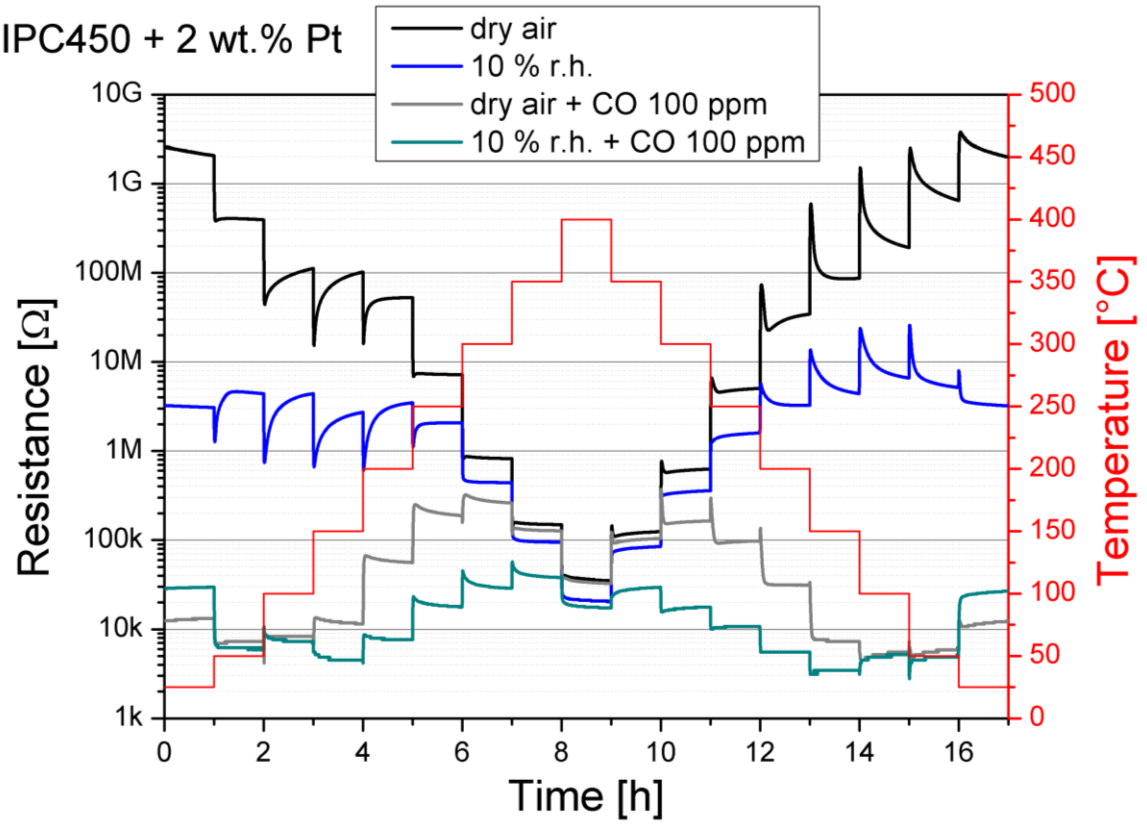

Figure 30: Overlay of 4 DC resistance measurements of Pt doped SnO_2 (IPC450). Sensor heating was programmed for a slow staircase from 25 °C to 400 °C and back down; step duration was 1 hour. Gas conditions changed for each run and are denoted in the legend.

In the center of the graph, temperature is at its maximum of 400 °C (hour 8 to 9) and therefore higher than what is generally considered ideal. Although humidity dependence was at its lowest (compare black to blue curve), so was its CO response, both in dry and humid background (compare black to grey and blue to cyan). Looking at 300 °C (hour 6 to 7 and 10 to 11), response to CO was quite

reasonable and within expected margin at that temperature. In humid conditions CO response was higher than in dry air; a trend that continued until somewhere in between 200-250 °C. For lower temperatures the response in dry air gained to upper hand and showed tremendously high values at 25 °C. Noteworthy was the appearance of overshoots upon temperature change in the 25 to 200 °C range. These got inverted during cool down and appeared in a similar range. Overshoots were way more pronounced for gas atmospheres without CO present, which indicated a faster time to reach equilibrium with a reducing gas present. H_2O alone didn't appear to be sufficient to suppress these overshoots.

Figure 31 illustrates the sensor signals calculated at each temperature of the upward and downward staircase by forming the ratio between resistances in the absence and in the presence of CO.

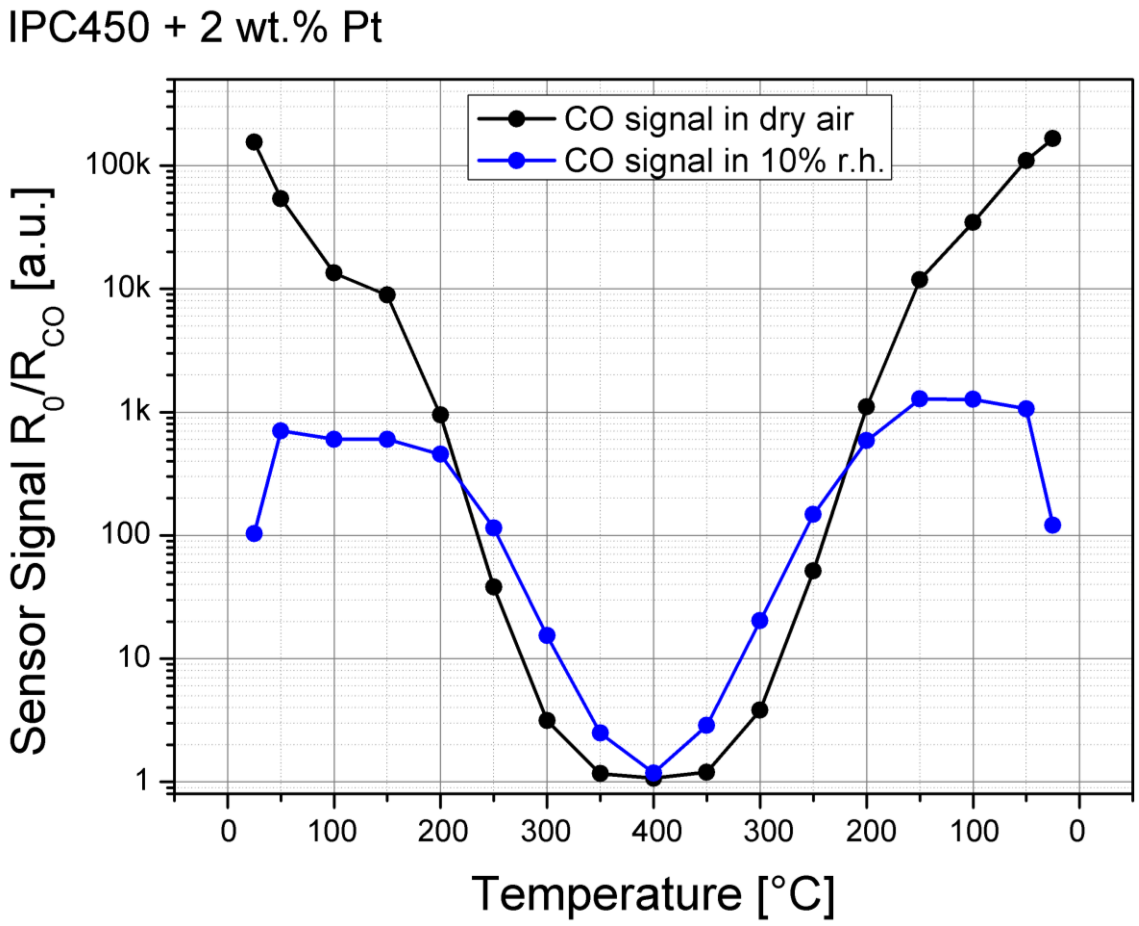

Figure 31: Calculated sensor signal for 100 ppm CO in a dry air background (black) and in humid air (blue). Resistance values for the calculation were extracted from data of Figure 30. Points were picked at the very end of each temperature step and the ratio between clean air and CO containing air was calculated and plotted.

In summary, sensor operation in a temperature modulated mode can significantly enhance gas responses, especially at lower temperatures. With regular heating intervals, the previously observed degradation of gas response over time can be mitigated fully. Even though it was not further investigated here, additional benefits of this mode lie within the opportunity to enhance gas selectivity. By screening through several temperatures, each target gas may result in a specific fingerprint, best evaluated with chemometric or machine learning methods.

It has been demonstrated that a suitable array of SMOX sensors with temperature modulated operation mode and sufficient amount of training data, is quite capable of identifying and quantifying individual gases in complex gas mixtures [83].

5.4 Nitrogen/Oxygen investigations

Temperature is known to play a primary role in the ability of metal oxides to interact with oxygen and consequently form ionosorbed species of it. The presences of ionosorbed, active oxygen at the surface of the metal oxide is essential for any interaction with reducing target gases that translate to changes in resistance. The degradation effect seen in the previous chapter could be understood as a gradual loss of active surface oxygen, resulting in reduced sensitivity to any reducing target gas. It could be assumed that within the first few hours after cool down a large amount of active oxygen – formed at 300 °C – is still present by “freezing out” this surface state. This state would deteriorate over time if the metal oxide is in fact unable to re-adsorb new oxygen at this low temperature.

In order to investigate the adsorption and desorption properties of the materials at different temperatures, the following experiment was conceived.

At the start of each sequence sensors were kept at 400 °C in a high flow rate of dry, high purity nitrogen (N6 – 1 ppm total impurities). After 4h in this condition the majority of active oxygen was considered to be desorbed and the metal oxide surface left in a highly reduced state. In the following 12h, the nitrogen flow was upheld, but sensor temperature was reduced to the desired value of 30, 70, 100, 130 or 300 °C and kept at that temperature for the remainder of the sequence. Those highly reduced sensors were then exposed to gas mixtures with increasing oxygen content ranging from 10 ppm up to 20.5% and then backwards down to 10 ppm.

During 400 °C heat-out in N_2 all investigated materials were in a strongly reduced state causing the resistance to stabilize in the single digit kOhm region. Upon cooling down to their respective temperature resulted in abrupt increases of resistance by up to 3 orders of magnitude. Depending on the actual temperature, reaching a state of equilibrium could take minutes, hours or even exceed the allotted 12 hours in this condition. The increase in resistance should mainly be attributed to the semiconductor aspect, meaning lower likelihood to populate conductive bands with decreasing temperature. As the gas condition was unchanged up to this point (dry N_2) the chemical composition of the surface could hardly be altered.

The introduction of O_2 to the gas mixture caused all materials at all temperatures to increase in resistance, whereas removal of O_2 provoked the opposite effect. With this the commonalities between the materials were already exhausted, mandating a per-material discussion.

Resistance data for pristine SnO_2 (IPC1000) is depicted in Figure 32, showing both the time resolved measurement data and the extracted resistances (at the end of each 2-hour exposure step) versus the present oxygen concentration. The sharp spikes visible in the upper plot between 160 ppm and 320 ppm, and between 1280 ppm and 5% were due to switches to another gas channel and associated impurities that may have accumulated in the channel while it was unused for several hours. Minor amounts of room air and therefore humidity could be the cause of those spikes. When working at extremely dry and oxygen free conditions even the smallest leakage in a temporarily unused channel can provoke an initially strong sensor reaction. Additionally, between 1280 ppm and 5% O_2, a different gas bottle is feeding the O_2 channel, which may introduce a small, but slightly different background level of humidity or other pollutants present in that bottle.

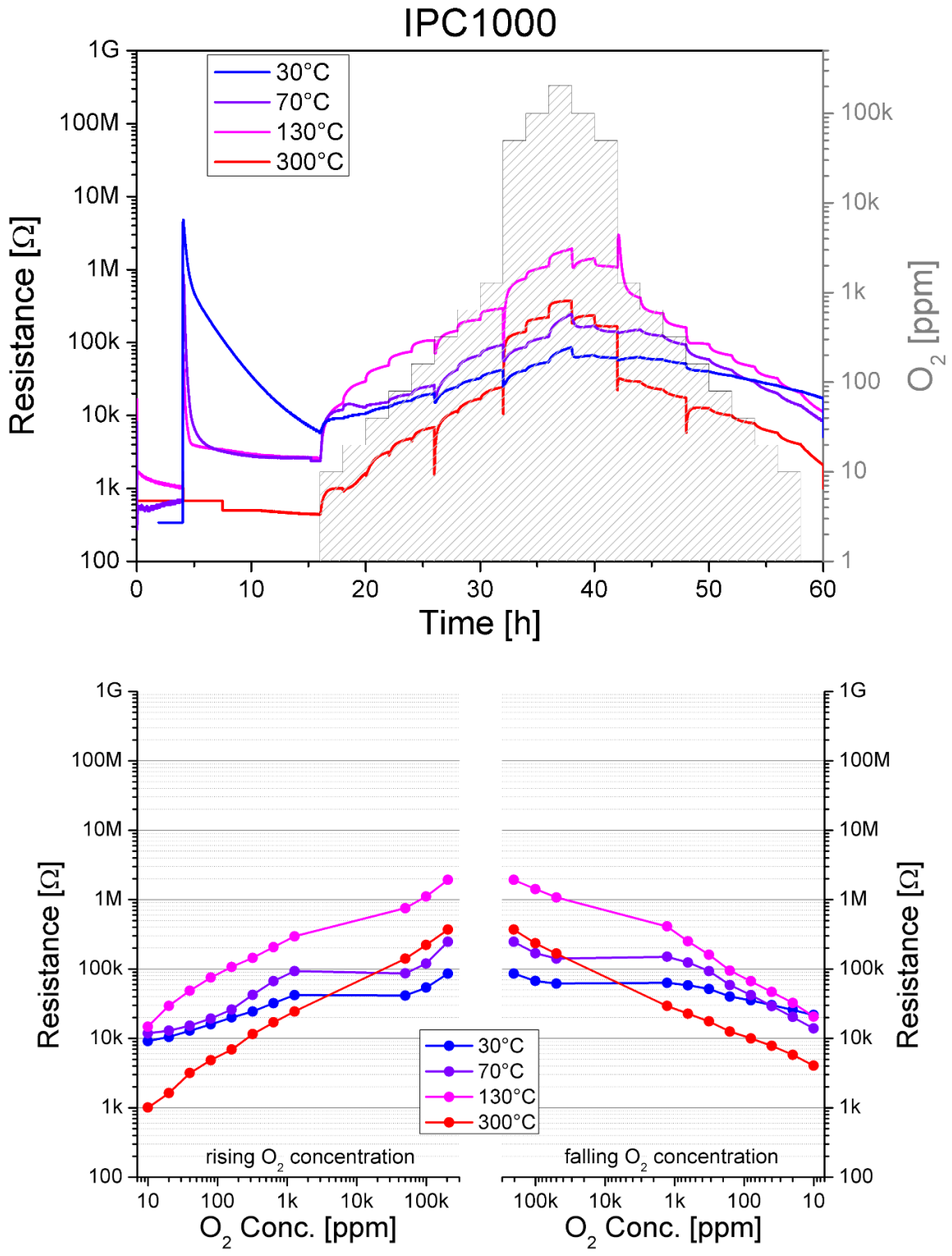

Figure 32: Top: DC resistance measurement of an undoped SnO_2 (IPC1000) sensor at different temperatures. At the start of each measurement the sensor was heated to 400°C in N_2 to deplete the surface of oxygen. Then it was cooled down and concentration ramps of oxygen were mixed in the gas flow. Bottom: Extracted resistances from each oxygen concentration, both for the rising and the falling ramps.

At 300 °C (red curve) the expected behavior upon oxygen exposure was registered. In the double logarithmic resistance vs. concentration plot a “linear” behavior was observed and the resistance was strongly increased by almost 3 orders of magnitude. With the high amount of thermal energy available the material was able to recover from the highly oxygen depleted state it had in N_2 atmosphere by dissociative adsorption of oxygen molecules and thereby healing most of its vacancies. When subsequently decreasing he oxygen concentration, the hysteresis loop was not very pronounced and resistances settled at only slightly higher values than for corresponding concentrations during increase. This was to be expected, as initial desorption of oxygen was performed at an even higher temperature of 400 °C for 4 hours in N_2. Oxygen absorption and desorption behavior at 300 °C was congruent with accepted models for metal oxide oxidation at that temperature. Data acquired at 130 °C showed quite comparable behavior. Resistance was overall higher but followed a similar trend when exposed to O_2. Literature would suggest that non-dissociative adsorption should dominate in this temperature regime and singly ionized O_2^- would outweigh other oxygen species like O^{2-}. In terms of resistance this would translate to a higher retention of free charge carriers and therefore the relative increase of resistances upon reaction with oxygen should be less pronounced as for 300 °C. For lower oxygen concentrations, no clear indication of this conduct was found in the measurement, but towards higher concentrations the relative resistance increase is lower than for 300 °C. At even lower temperatures, namely 70 °C and 30 °C, interaction with oxygen should be limited to physisorption and some degree of ionization to O_2^-. This was reflected in the resistance changes, who were much smaller than at higher temperatures, but present none the less. Would there be no ionization happening, the resistance would remain unchanged. The implication being that pristine SnO_2 is capable of oxygen interaction, accompanied by resistance increase, even at 30 °C. Desorption capability of O_2 was also observed, although the process was slow and incomplete at temperatures close to RT.

Moving on to Pd doped SnO_2 (Figure 33) presented quite a different picture for oxygen interaction, especially for the two lowest temperatures. Response at 300 °C was the most comparable scenario and similar to pristine SnO_2. Resistance increased fast and steady upon increasing O_2 levels and no notable hysteresis could be observed. Generally, Pd doping shifted resistances to higher values for all

temperatures. 130 °C was qualitatively comparable to the undoped variant with its fast and strong responses to O_2. It should be noted that the switch from 1280 ppm to 5% O_2 introduces a sharp initial resistance drop which most likely stems from the concurrently changed gas channel. Each gas bottle has slightly different level of residual humidity as a contaminant and can impact the resistance more or less. For the Pd doped material and at lower temperatures this effect appeared to be magnified and lead to actually lower resistances at 5% than at 1280 ppm O_2, which is obviously counterintuitive. Results for 5%, 10% and 20.5% O_2 should therefore be taken with a grain of salt. At temperatures of 70 °C and 30 °C the difference compared to undoped material was the most profound. Pd doping enabled the material to interact more easily with O_2, as seen by the severe increase of resistance over more than 2 decades. When analyzing the trend for falling O_2 concentrations the Pd doping did not provide any benefit to the desorption rate and to be precise, even slowed it down for 30 °C were resistance drops down not even a full decade after an initial rise over more than 2 decades.

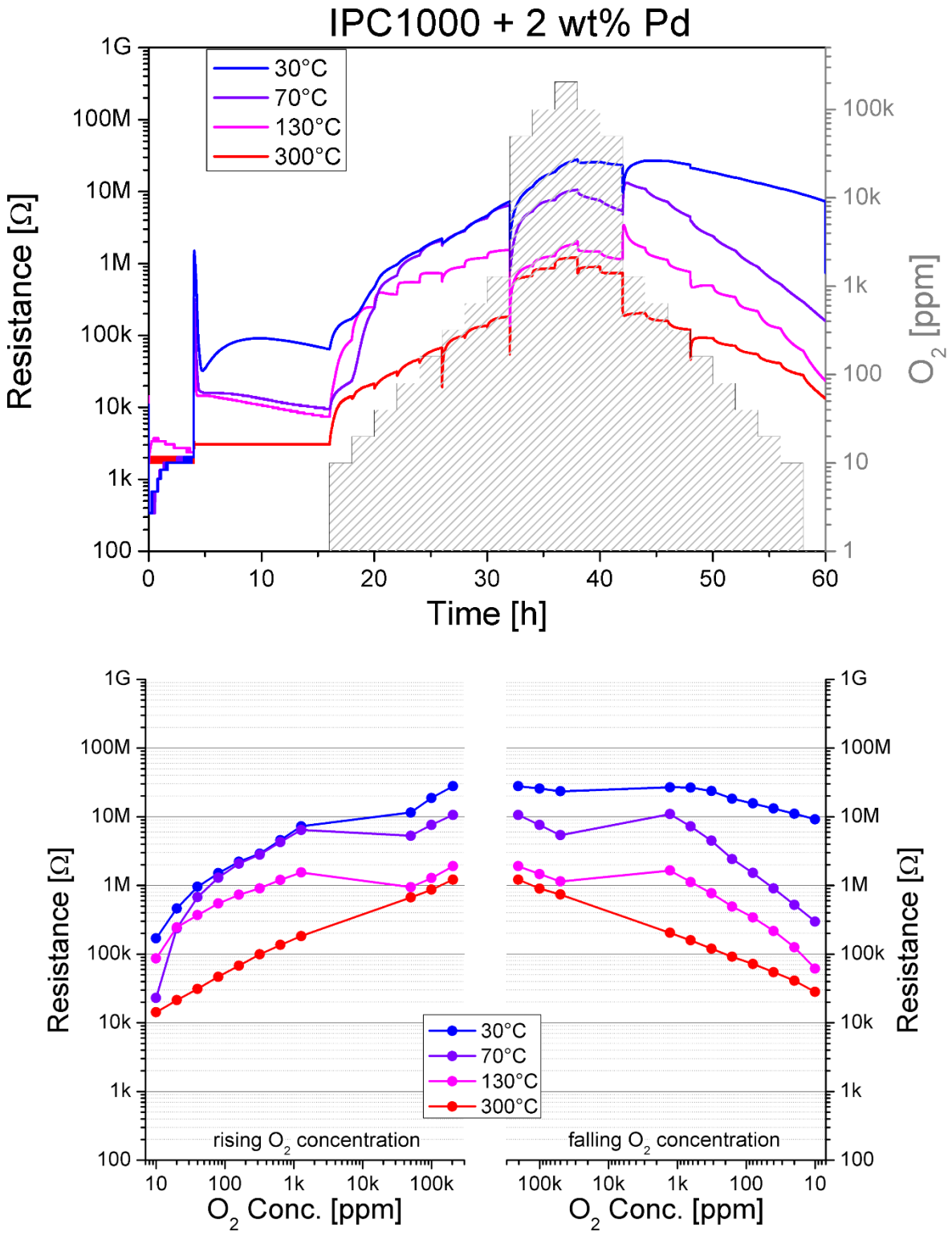

Figure 33: Top: DC resistance measurement of a Pd doped SnO_2 (IPC1000) sensor at different temperatures. At the start of each measurement the sensor was heated to 400°C in N_2 to deplete the surface of oxygen. Then it was cooled down and concentration ramps of oxygen were mixed in the gas flow. Bottom: Extracted resistances from each oxygen concentration, both for the rising and the falling ramps.

The results of Pt doped SnO_2 are shown in Figure 34 below. The overall trends were comparable to Pd doped behavior, but effect of oxygen uptake at lower temperatures was clearly magnified. At 30 °C even the lowest concentration of O_2 caused a very strong increase of resistance and at 20.5% O_2 this expressed itself as more than 4 decades difference to the N_2 level. Contrary to Pd doping, the presence of Pt seemed to enhance O_2 desorption capabilities at 30 °C, as could be seen by the sharp resistance decrease for falling O_2 concentrations. The other temperatures showed less pronounced differences to the previous material and behaved qualitatively the same.

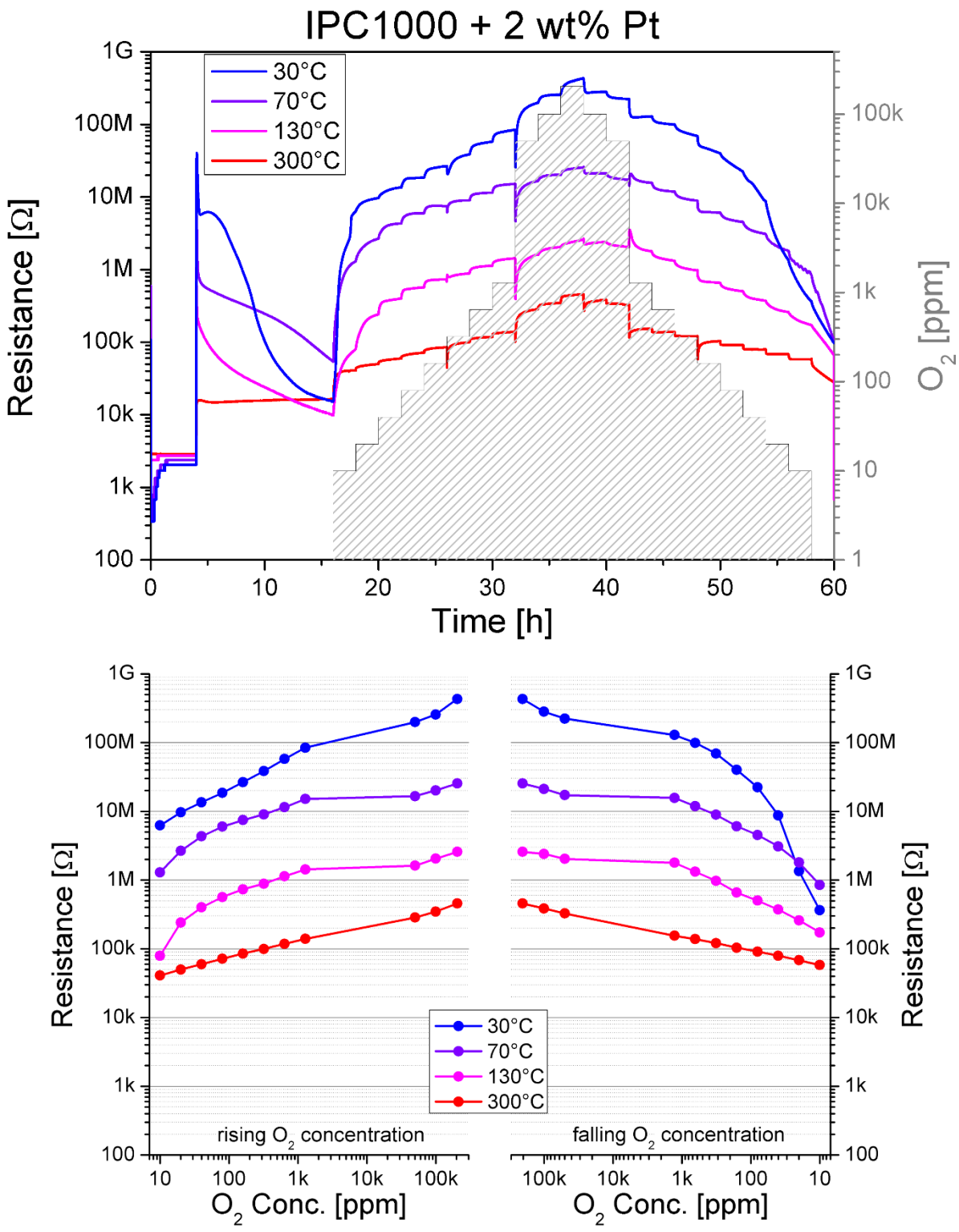

Figure 34: Top: DC resistance measurement of a Pt doped SnO_2 (IPC1000) sensor at different temperatures. At the start of each measurement the sensor was heated to 400°C in N_2 to deplete the surface of oxygen. Then it was cooled down and concentration ramps of oxygen were mixed in the gas flow. Bottom: Extracted resistances from each oxygen concentration, both for the rising and the falling ramps.

Another way to present the data is depicted in Figure 35, where ratios between the resistances under oxygen exposure and their respective N_2 level were calculated and plotted versus the oxygen concentration. Besides plots for the individual materials, the fourth plot highlights the 30 °C curves of all materials.

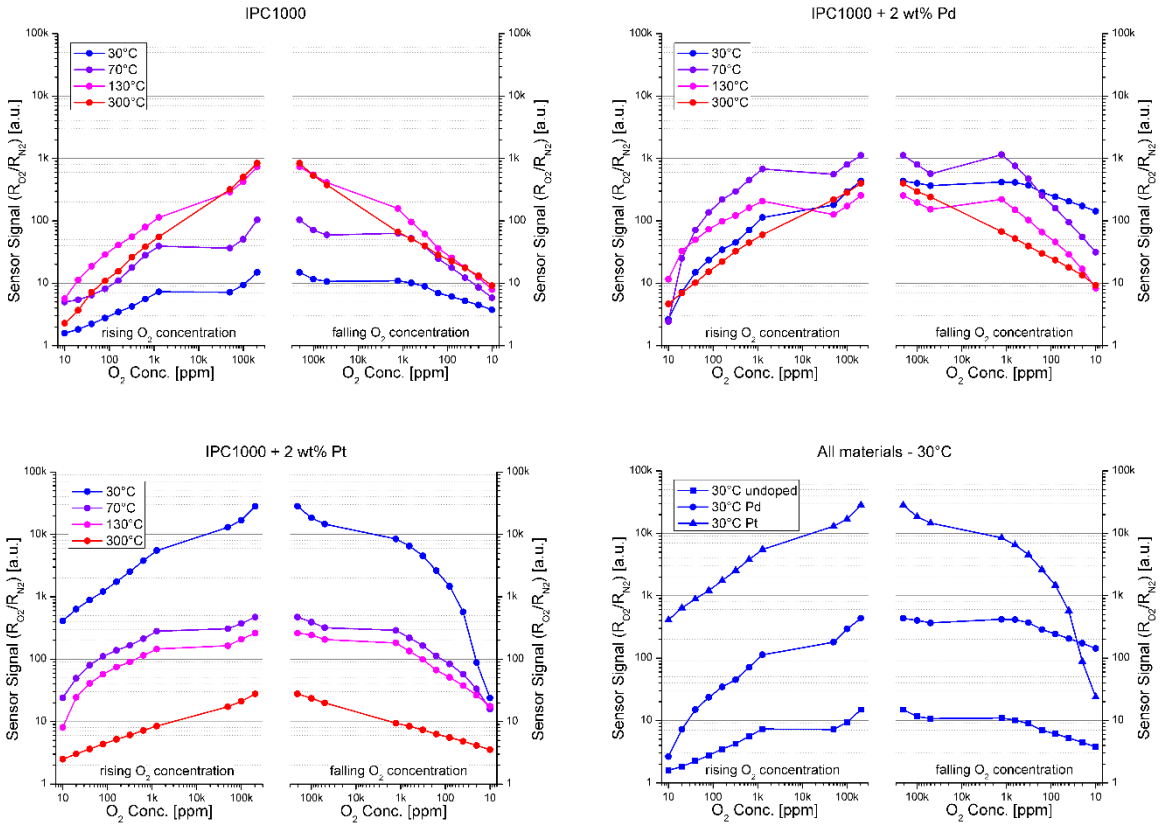

Figure 35: Calculated sensor signals versus oxygen concentration for all three sensors at all tested temperatures and, at the bottom right, an overlay of the results at 30°C.

Undoped SnO_2 showed the largest relative changes of resistance for 130 °C and 300 °C while lower temperatures had weaker signals. At 30 °C signals were barely exceeding a value of 10 whereas the 300 °C values approaches 1000, indicating a limit capability of the material to interact with oxygen in a way that it translates to electronical changes at low temperatures.

The addition of Pd to the material painted a different picture to oxygen adsorption capabilities, as the signals for 300 °C and 30 °C are almost identical. This was caused by significantly stronger responses at 30 °C. Desorption capabilities were, on the other hand, very limited at that temperature. Benefits could also be observed for 70 °C which achieved the highest signals for the here tested temperatures.

The view on sensor signals also highlighted the impact of Pt doping on the oxygen interaction at low temperatures. A signal of ~30,000 at 20.5% oxygen concentration was a testament to the ability of this material to effectively react with oxygen without much need for thermal excitation.

Focusing the comparison on 30 °C measurements reveals the effect of doping on oxygen adsorption and desorption capabilities of SnO_2. As the electrode structure of the sensors was made out of Pt, all tested materials had some contact to this metal and could profit from its presence. But an additional doping of the material itself with Pd or Pt increased the contact area of those metal to the atmosphere significantly and provided further enhancements.

6. Summary

For this work two variants of SnO_2 nanomaterials were synthesized and decorated with Pd and Pt particles via powder impregnation. Initial DC resistance measurements indicated decent sensor performance at low temperatures, but also revealed a strong dependence on the recent temperature history of the specific sensor. This decay of sensor performance was investigated in more detail and was complemented with operando infrared spectroscopy to better understand the proceedings.

The operando studies included time resolved investigations into the behavior of the baseline and under CO and H_2 exposure. While the formation of a water layer and its impact on CO and H_2 sensing was already reported upon in previous works of this research group, its appearance could be confirmed in this work. As the main novel aspect, oxygen and its transformation to the molecularly ionosorbed form was attributed the key role in the degrading responsiveness to target gases for SnO_2 materials at prolonged operation at room temperature. The addition of metal dopants to the material did not result in a perpetuation of sensor properties but their spectra instead also bore the appearance of this characteristic molecular oxygen peak.

The assumed mechanism for CO detection at RT was found to be no different than at elevated temperatures, as the same Sn-O bonds got reduced whereas the O_2^- signals didn’t change at all, making them unsuited for CO interaction and effectively block an oxygen site with an unreactive variant. CO_2 generation could not be

observed though, indicating a low turnover rate that stayed invisible in the spectra. The signals for OH groups were also altered upon CO exposure in a comparable manner to high temperature conditions. Different were changes in interaction with adsorbed water, which in the first place only appeared at temperatures below 100 °C and only then a decrease of this interaction could be observed, and changes in the rooted OH groups which decreased when CO was present. After a prolonged time at RT (2 days) all signals in the spectrum were significantly lowered and correlated with the electronical signals.

For H_2 similar results were found. Reduction of the surface could be observed, indicating a reaction with ionosorbed oxygen. The molecular O_2^- species was not involved in the reaction. Hydroxyl groups and water signals got diminished upon H_2 interaction, just as they were for CO exposure. In summary the decay of signals over time was attributed to the decreasing availability of reactive oxygen species and continued build-up of water related hydroxyl groups.

Sensor performance for H_2 gas at low temperatures:

An investigation into reproduceable H_2 responses was performed with defined heat out settings, a long baseline equilibration phase and a fixed H_2 concentration event. The results for the six tested sensor materials could be split up into two groups, doped and undoped variants. The former started with low responses at RT but steadily increased and peaked at an intermediate temperature. The latter peaked at RT, but dropped sharply at intermediate thermals, then increased their values again towards respectable performance at 300 °C.

The main proposition of this experiment is proof of the ability of these materials to deliver strong and repeatable sensor signals, if regular heating intervals are provided and the low temperature is chosen with knowledge of the material and target gas.

Temperature modulated operation mode:

A logical extension of the previous approach of oscillating between just two temperatures, is the expansion to multiple temperature steps and exploiting the sensors capabilities fully. Demonstrated here, was the performance of a doped

SnO_2 material in regards to CO detection in dry and humid conditions, which resulted in excellent sensor signals to this target gas.

Nitrogen/Oxygen uptake measurements:

The tested scenario investigated the ability of highly reduced SnO_2 to bind to oxygen at varying temperatures and observe the resulting resistance changes. It was shown that over the full temperature range absorption of oxygen and the associated resistance increase is occurring. Even though at RT only molecular adsorption is expected, the impact on resistance was quite significant. The usefulness of this oxygen species for reaction with analyte gases like CO and H_2 however is low, as it was revealed in the IR investigations of this work.

Bibliography

[1] J. Haldane, "The Action of Carbonic Oxide on Man," *The Journal of Physiology,* vol. 18, no. 5-6, p. 430–462, 1895.

[2] H. Davy, "On the fire-damp of coal mines, and on methods of lighting the mines so as to prevent its explosion," *Philosophical Transactions of the Royal Society of London,* vol. 106, pp. 1-22, 1816.

[3] K. Matthes, "Untersuchungen über die Sauerstoffsättigung des menschlichen Arterienblutes," *Naunyn-Schmiedeberg's Archives of Pharmacology,* vol. 179, no. 6, pp. 698-711, 1935.

[4] J. W. Severinghaus and Y. Honda, "History of blood gas analysis. VII. Pulse oximetry," *Journal of Clinical Monitoring,* vol. 3, no. 2, pp. 135-138, 1987.

[5] L. C. Clark, R. Wolf, D. Granger and Z. Taylor, "Continuous Recording of Blood Oxygen Tensions by Polarography," *Journal of Applied Physiology,* vol. 6, no. 3, pp. 189-193, 1953.

[6] W. H. Brattain and J. Bardeen, "Surface Properties of Germanium," *Bell System Technical Journal,* vol. 32, no. 1, pp. 1-41, 1953.

[7] G. Heiland, "Zum Einfluß von adsorbiertem Sauerstoff auf die elektrische Leitfähigkeit von Zinkoxydkristallen," *Zeitschrift für Physik,* vol. 138, p. 459–464, 1954.

[8] A. Bielanski, J. Deren and J. Haber, "Electric Conductivity and Catalytic Activity of Semiconducting Oxide Catalysts," *Nature,* vol. 179, p. 668–669, 1957.

[9] T. Seiyama, A. Kato, K. Fujiishi and M. Nagatani, "A new detector for gaseous components using semiconductive thin films," *Analytical Chemistry,* vol. 34, no. 11, pp. 1502-1503, 1962.

[10] N. Taguchi, "GAS DETECTING DEVICE". United States of America Patent 3631436A, 28 December 1971.

[11] N. Taguchi, "GAS DETECTING DEVICE". United States of America Patent 3695848A, 3 October 1972.

[12] Caterpillar, "catphones.com," [Online]. Available: https://www.catphones.com/download/User-Manuals/S61-Smartphone/S61-User-Manual-English.pdf. [Accessed 01 10 2024].

[13] A. Staerz, U. Weimar and N. Barsan, "Current state of knowledge on the metal oxide based gas sensing mechanism," *Sensors and Actuators B: Chemical,* vol. 358, p. 131531, 2022.

[14] Z. Wang, A. Sackmann, S. Gao, U. Weimar, G. Lu, S. Liu and T. Zhang, "Study on highly selective sensing behavior of ppb-level oxidizing gas sensors," *Sensors and Actuators B: Chemical,* vol. 285, pp. 590-600, 2019.

[15] T. Fu, "Research on gas-sensing properties of lead sulfide-based sensor for detection of NO2 and NH3 at room temperature," *Sensors and Actuators B: Chemical,* vol. 140, no. 1, pp. 116-121, 2009.

[16] E. Ogel, S. A. Müller, A. Sackmann, F. Gyger, P. Bockstaller, E. Brose, M. Casapu, L. Schöttner, D. Gerthsen, K. Feldmann and J.-D. Grunwaldt, "Comparison of the Catalytic Performance and Carbon Monoxide Sensing Behavior of Pd-SnO2 Core@Shell Nanocomposites," *ChemCatChem Communications,* vol. 9, pp. 407-413, 2017.

[17] B. Junker, A. Kobald, C. Ewald, P. Janoschek, M. Schalk, U. Weimar, L. Mädler and N. Barsan, "Multivariate Analysis of Light-Activated SMOX Gas Sensors," *ACS Sensors,* vol. 9, pp. 1584-1591, 2024.

[18] Figaro, "Datasheet TGS2442," [Online]. Available: https://cdn.soselectronic.com/productdata/af/2e/9901fb15/tgs-2442.pdf. [Accessed 1 10 2024].

[19] D. Degler, Spectroscopic insights in the gas detection mechanism of tin dioxide based gas sensors, Dissertation: Eberhard Karls University of Tübingen, 2017.

[20] Z. Li, H. Li, Z. Wu, M. Wang, J. Luo, H. Torun, P. Hu, C. Yang, M. Grundmann, X. Liu and Y. Fu, "Advances in designs and mechanisms of semiconducting metal oxide nanostructures for high-precision gas sensors operated at room temperature," *Materials Horizons,* vol. 6, pp. 470-506, 2019.

[21] N. Zhang, K. Yu, Q. Li, Z. Q. Zhu and Q. Wan, "Room-temperature high-sensitivity H2S gas sensor based on dendritic ZnO nanostructures with macroscale in appearance," *Journal of Applied Physics,* vol. 103, p. 104305, 2008.

[22] Z. Li, S. Yan, S. Zhang, J. Wang, W. Shen, Z. Wang and Y. Q. Fu, "Ultra-sensitive UV and H2S dual functional sensors based on porous In2O3 nanoparticles operated at room temperature," *Journal of Alloys and Compounds,* vol. 770, pp. 721-731, 2019.

[23] Z. Li, X. Niu, Z. Lin, N. Wang, H. Shen, W. Liu, K. Sun, Y. Q. Fu and Z. Wang, "Hydrothermally synthesized CeO2 nanowires for H2S sensing at room temperature," *Journal of Alloys and Compounds,* vol. 682, pp. 647-653, 2016.

[24] Y. Huang, W. Chen, S. Zhang, Z. Kuang, D. Ao, N. R. Alkurd, W. Zhou, W. Liu, W. Shen and Z. Li, "A high performance hydrogen sulfide gas sensor based on porous α-Fe2O3 operates at room-temperature," *Applied Surface Science,* vol. 351, pp. 1025-1033, 2015.

[25] J. J. Hassan, M. A. Mahdi, C. W. Chin, H. Abu-Hassan and Z. Hassan, "A high-sensitivity room-temperature hydrogen gas sensor based on oblique and vertical ZnO nanorod arrays," *Sensors and Actuators B: Chemical,* vol. 176, pp. 360-367, 2013.

[26] M. Kodu, T. Avarmaa, A. Floren and R. Jaaniso, "Bias dependent NO2 sensitivity of SnO2 thin films at room temperature," *Journal of the European Ceramic Society,* vol. 33, no. 12, pp. 2335-2340, 2013.

[27] R. Chen, J. Wang and L. Xiang, "Facile synthesis of mesoporous ZnO sheets assembled by small nanoparticles for enhanced NO2 sensing performance at room temperature," *Sensors and Actuators B: Chemical,* vol. 270, pp. 207-215, 2018.

[28] X. Mu, C. Chen, L. Han, B. Shao, Y. Wei, Q. Liu and P. Zhu, "Indium oxide octahedrons based on sol–gel process enhance room temperature gas sensing performance," *Journal of Alloys and Compounds,* vol. 637, pp. 55-61, 2015.

[29] N. Du, H. Zhang, B. D. Chen, X. Y. Ma, Z. H. Liu, J. B. Wu and D. R. Yang, "Porous Indium Oxide Nanotubes: Layer-by-Layer Assembly on Carbon-Nanotube Templates and Application for Room-Temperature NH3 Gas Sensors," *Advanced Materials,* vol. 19, no. 12, pp. 1641-1645, 2007.

[30] A. P. Sharma, P. Dhakal, D. K. Pradhan, M. K. Behera, B. Xiao and M. Bahoura, "Fabrication and characterization of SnO2 nanorods for room temperature gas sensors," *AIP Advances,* vol. 8, p. 095219, 2018.

[31] M. Seetha, P. Meena, D. Mangalaraj, Y. Masuda and K. Senthil, "Synthesis of indium oxide cubic crystals by modified hydrothermal route for application in room temperature flexible ethanol sensors," *Materials Chemistry and Physics,* vol. 133, no. 1, pp. 47-54, 2012.

[32] R. Senthilkumar, G. Ravi, C. Sanjeeviraja, M. Arivanandhan and Y. Hayakawa, "Room temperature ethanol sensing property of cubic nanostructure tungsten oxide (WO3)," *AIP Conference Proceedings,* vol. 1512, p. 648–649, 2013.

[33] M. J. Lee, J.-E. Park, S. Kim, S. Kim, E. Lee, S.-J. Kim and W. Lee, "Ultra-sensitive hydrogen gas sensors based on Pd-decorated tin dioxide nanostructures: Room temperature operating sensors," *International Journal of Hydrogen Energy,* vol. 35, no. 22, pp. 12568-12573, 2010.

[34] S.-C. Wang and M. O. Shaikh, "A Room Temperature H2 Sensor Fabricated Using High Performance Pt-Loaded SnO2 Nanoparticles," *Sensors,* vol. 15, no. 6, pp. 14286-14297, 2015.

[35] P. Manjula, S. Arunkumar and S. V. Manorama, "Au/SnO2 an excellent material for room temperature carbon monoxide sensing," *Sensors and Actuators B: Chemical,* vol. 152, pp. 168-175, 2011.

[36] S. Arunkumar, T. Hou, Y.-B. Kim, B. Choi, S. H. Park, S. Jung and D.-W. Lee, "Au Decorated ZnO hierarchical architectures: Facile synthesis, tunable morphology and

enhanced CO detection at room temperature," *Sensors and Actuators B: Chemical,* vol. 243, pp. 990-1001, 2017.

[37] S. Ren, G. Fan, S. Qu and Q. Wang, "Enhanced H2 sensitivity at room temperature of ZnO nanowires functionalized by Pd nanoparticles," *Journal of Applied Physics,* vol. 110, p. 084312, 2011.

[38] K. Wang, T. Zhao, G. Lian, Q. Yu, C. Luan, Q. Wang and D. Cui, "Room temperature CO sensor fabricated from Pt-loaded SnO2 porous nanosolid," *Sensors and Actuators B: Chemical,* vol. 184, pp. 33-39, 2013.

[39] O. Lupan, V. Postica, F. Labat, I. Ciofini, T. Pauporte and R. Adelung, "Ultra-sensitive and selective hydrogen nanosensor with fast response at room temperature based on a single Pd/ZnO nanowire," *Sensors and Actuators B: Chemical,* vol. 254, pp. 1259-1270, 2018.

[40] A. Sackmann, Low temperature properties of SnO2 based material for CO and H2 gas sensing, Diploma thesis: Eberhard Karls University of Tübingen, 2014.

[41] W. H. Baur, "Über die Verfeinerung der Kristallstrukturbestimmung einiger Vertreter des Rutiltyps: TiO2, SnO2, GeO2 und MgF2," *Acta Crystallographica,* vol. 9, no. 6, pp. 515-520, 1956.

[42] Z. M. Jarzebski, "Physical Properties of SnO2 Materials," *Journal of The Electrochemical Society,* vol. 123, no. 7, pp. 299-310, 1976.

[43] S. Munnix and M. Schmeits, "Electronic structure of tin dioxide surfaces," *Physical Review B,* vol. 27, no. 12, p. 7624–7635, 1983.

[44] S. Samson and C. G. Fonstad, "Defect structure and electronic donor levels in stannic oxide crystals," *Journal of Applied Physics,* vol. 44, no. 10, pp. 4618-4621, 1973.

[45] B. Kamp, R. Merkle and J. Maier, "Chemical diffusion of oxygen in tin dioxide," *Sensors and Actuators B: Chemical,* vol. 77, no. 1-2, pp. 534-542, 2001.

[46] D. S. Ginley and J. D. Perkins, Transparent Conductors, Boston, MA: Springer, 2010.

[47] J. Mohelníková, Window Glass Coatings, London: Springer, 2011.

[48] P. Mars and D. W. van Krevelen, "Oxidations carried out by means of vanadium oxide catalysts," *Special Supplement to Chemical Engineering Science,* vol. 3, pp. 41-59, 1954.

[49] N. Barsan and U. Weimar, "Conduction Model of Metal Oxide Gas Sensors," *Journal of Electroceramics,* vol. 7, pp. 143-167, 2001.

[50] D. Kohl, "Surface processes in the dectection of reducing gases with SnO2-based devices," *Sensors and Actuators,* vol. 18, no. 1, pp. 71-113, 1989.

[51] U. Pulkkinen, T. T. Rantala, T. S. Rantala and V. Lantto, "Simulation of oxygen exchange of SnO2 surface," *Computer Physics Communications,* vol. 121, p. 720, 1999.

[52] J.-M. Ducréré, A. Hemeryck, A. Estève, M. D. Rouhani, G. Landa, P. Ménini, C. Tropis, A. Maisonnat and B. Chaudret, "A computational chemist approach to gas sensors: Modeling the response of SnO2 to CO, O2, and H2O Gases," *Journal of Computational Chemistry,* vol. 33, no. 3, pp. 247-258, 2012.

[53] S. Saukko, U. Lassi, V. Lantto, M. Kroneld, S. Novikov, P. Kuivalainen, T. T. Rantala and J. Mizsei, "Experimental studies of O2–SnO2 surface interaction using powder, thick films and monocrystalline thin films," *Thin Solid Films,* vol. 490, no. 1, pp. 48-53, 2005.

[54] S.-C. Chang, "Oxygen chemisorption on tin oxide: Correlation between electrical conductivity and EPR measurements," *Journal of Vacuum Science & Technology,* vol. 17, no. 1, pp. 366-369, 1980.

[55] S. Lenaerts, J. Roggen and G. Maes, "FT-IR characterization of tin dioxide gas sensor materials under working conditions," *Spectrochimica Acta Part A: Molecular and Biomolecular Spectroscopy,* vol. 51, no. 5, pp. 883-894, 1995.

[56] A. V. Marikutsa, M. N. Rumyantseva, D. D. Frolov, M. I. V, A. I. Boltalin, A. A. Fedorova, I. A. Petukhov, L. V. Yashina, K. E. A, S. E. M, A. M. Abakumov, Z. Y. V and G. A. M, "Role of PdO x and RuO y Clusters in Oxygen Exchange between Nanocrystalline Tin Dioxide and the Gas Phase," *The Journal of Physical Chemistry,* vol. 117, no. 45, pp. 23858-23867, 2013.

[57] S. R. Morrison, The Chemical Physics of Surfaces, New York: Plenum Press, 1977.

[58] N. Yamazoe, J. Fuchigami, M. Kishikawa and T. Seiyama, "Interactions of tin oxide surface with O2, H2O and H2," *Surface Science,* vol. 86, pp. 335-344, 1979.

[59] E. W. Thornton and P. G. Harrison, "Part 1. - Surface Hydroxyl Groups and the Chemisorption of Carbon Dioxide and Carbon Monoxide on Tin(IV) Oxide," *Journal of the Chemical Society, Faraday Transactions 1: Physical Chemistry in Condensed Phases,* vol. 71, pp. 461-472, 1975.

[60] M. Egashlra, M. Nakashlma and S. Kawasuml, "Temperature Programmed Desorption Study of Water Adsorbed on Metal Oxides. 2. Tin Oxide Surfaces," *The Journal of Physical Chemistry,* vol. 85, no. 26, pp. 4125-4130, 1981.

[61] P. G. Harrison and A. Guest, "Tin oxide surfaces. Part 17. - An infrared and thermogravimetric analysis of the thermal dehydration of tin(IV) oxide gel," *Journal of the Chemical Society, Faraday Transactions 1: Physical Chemistry in Condensed Phases,* vol. 83, no. 11, pp. 3383-3397, 1987.

[62] S. Wicker, Influence of humidity on the gas sensing characteristics of SnO2 - DRIFTS investigation of different base materials and dopants, Dissertation: Eberhard Karls University Tübingen, 2016.

[63] V. E. Heinrich and P. A. Cox, Surface Science of Metal Oxides, 1st edition, Cambridge University Press, 1994.

[64] N. Yamazoe, K. Suematsu and K. Shimanoe, "Two types of moisture effects on the receptor function of neat tin oxide gas sensor to oxygen," *Sensors and Actuators B: Chemical,* vol. 176, pp. 443-452, 2013.

[65] G. Santarossa, K. Hahn and A. Baiker, "Free energy and electronic properties of water adsorption on the SnO2 (110) surface," *Langmuir,* vol. 29, no. 18, pp. 5487-5499, 2013.

[66] V. A. Gercher and D. F. Cox, "Water adsorption on stoichiometric and defective SnO2 (110) surfaces," *Surface science,* vol. 322, no. 1-3, pp. 177-184, 1995.

[67] M. Batzill, W. Bergermayer, I. Tanaka and U. Diebold, "Tuning the chemical functionality of a gas sensitive material: water adsorption on SnO2 (101)," *Surface science,* vol. 600, no. 4, pp. 29-32, 2006.

[68] D. Koziej, K. Thomas, N. Barsan, F. Thibault-Starzyk and U. Weimar, "Influence of annealing temperature on the CO sensing mechanism for tin dioxide based sensors–Operando studies," *Catalysis today,* vol. 126, no. 1-2, pp. 211-218, 2007.

[69] P. G. Harrison and A. Guest, "Tin oxide surfaces. Part 18. - Infrared study of the adsorption of very low levels (20–50 ppm) of carbon monoxide in air on to tin (IV) oxide gel," *Journal of the Chemical Society, Faraday Transactions 1: Physical Chemistry in Condensed Phases,* vol. 85, no. 8, pp. 1897-1906, 1989.

[70] D. Amalric-Popescu and F. Bozon-Verduraz, "Infrared studies on SnO2 and Pd/SnO2," *Catalysis today,* vol. 70, no. 1-3, pp. 139-154, 2001.

[71] X. Wang, H. Qin, Y. Chen and J. Hu, "Sensing mechanism of SnO2 (110) surface to CO: density functional theory calculations," *The Journal of Physical Chemistry C,* vol. 118, no. 49, pp. 28548-28561, 2014.

[72] N. Sergent, P. Gélin, Périer-Camby, P. H. and G. Thomas, "FTIR study of low-temperature CO adsorption on high surface area tin (IV) oxide: probing Lewis and Brønsted acidity," *Physical Chemistry Chemical Physics,* vol. 4, no. 19, pp. 4802-4808, 2002.

[73] U. Weimar, Gas Sensing with Tin Oxide: Elementary Steps and Signal Transduction, Habilitation: Eberhard Karls University of Tübingen, 2001.

[74] I. Barin, O. Knacke and O. Kubaschewski, Thermochemical properties of inorganic substances, Berlin, Heidelberg: Springer, 1977.

[75] M. Hübner, New Approaches for the Basic Understanding of Semiconducting Metal Oxide Based Gas Sensors: Sensing, Transduction and Appropriate Modeling, Dissertation: Eberhard Karls University of Tübingen, 2011.

[76] N. Yamazoe, Y. Kurokawa and T. Seiyama, "Effects of additives on semiconductor gas sensors," *Sensors and Actuators,* vol. 4, pp. 283-289, 1983.

[77] S. Matsushima, Y. Teraoka, N. Miura and N. Yamazoe, "Electronic interaction between metal additives and tin dioxide in tin dioxide-based gas sensors," *Japanese journal of applied physics,* vol. 27, no. 10R, pp. 1798-1802, 1988.

[78] M. Hübner, D. Koziej, J. D. Grunwaldt, U. Weimar and N. Barsan, "An Au clusters related spill-over sensitization mechanism in SnO 2-based gas sensors identified by operando HERFD-XAS, work function changes, DC resistance and catalytic conversion studies," *Physical Chemistry Chemical Physics,* vol. 14, no. 38, pp. 13249-13254, 2012.

[79] J. Kappler, Characterisation of high-performance SnO2 gas sensors for CO detection by in situ techniques, Dissertation: Eberhard Karls University of Tübingen, 2001.

[80] A. Dieguez, A. Romano-Rodríguez, J. R. Morante, J. Kappler, N. Barsan and W. Göpel, "Nanoparticle engineering for gas sensor optimisation: improved sol–gel fabricated nanocrystalline SnO2 thick film gas sensor for NO2 detection by calcination, catalytic metal introduction and grinding treatments," *Sensors and Actuators B: Chemical,* vol. 60, no. 2-3, pp. 125-137, 1999.

[81] A. Davydov, Molecular spectroscopy of oxide catalyst surfaces, Chichester: Wiley, 2003.

[82] F. C. Meunier, "Relevance of IR Spectroscopy of Adsorbed CO for the Characterization of Heterogeneous Catalysts Containing Isolated Atoms," *The Journal of Physical Chemistry C,* vol. 125, no. 40, pp. 21810-21823, 2021.

[83] A. Kobald, U. Weimar and N. Barsan, "Regression model for the prediction of pollutant gas concentrations with temperature modulated gas sensors," *IEEE International Symposium on Olfaction and Electronic Nose (ISOEN),* pp. 1-3, 2022.

List of Figures

List of publications

Articles in peer reviewed journals:

- M. Hübner, A. Sackmann, F. Gyger, P. Bockstaller, D. Gerthsen, U. Weimar and N. Barsan, "Location effect of Pd additives on the detection of reducing gases for nanoscale SnO_2 hollow spheres based gas sensors," *Procedia Engineering*, vol. 47, pp. 208-211, 2012.
- F. Gyger, A. Sackmann, M. Hübner, P. Bockstaller, D. Gerthsen, H. Lichtenberg, J.-D. Grunwaldt, N. Barsan, U. Weimar and C. Feldmann, "Pd@SnO_2 and SnO_2@Pd core@shell nanocomposite sensors," *Particle & Particle Systems Characterization*, vol. 31, no. 5, pp. 591-596, 2014.
- C. E. Simion, A. Sackmann, V. S. Teodorescu, C. F. Rusti, R. M. Piticescu and A. Stanoiu, "Tuned sensitivity towards H_2S and NH_3 with Cu doped barium strontium titanate materials," *AIP Conference Proceedings*, vol. 1627, no. 1, pp. 92-97, American Institute of Physics, 2014.
- S. Somacescu, P. Osiceanu, J. M. Calderon-Moreno, A. Sackmann, C. E. Simion and A. Stanoiu, "Mesopororous $Sn_{0.9-x}In_{0.1}Cu_x^{(I)}O_{2-\delta}$ gas sensors with selectivity to H_2S working under humid air conditions," *Microporous and mesoporous materials*, vol. 197, pp. 63-71, 2014.
- C. E. Simion, A. Sackmann, V. S. Teodorescu, C. F. Rusti and A. Stanoiu, "Room temperature ammonia sensing with barium strontium titanate under humid air background," *Sensors and Actuators B: Chemical*, vol. 220, pp. 1241-1246, 2015.
- A. Stanoiu, S. Somacescu, J. M. Calderon-Moreno, V. S. Teodorescu, O. G. Florea, A. Sackmann and C. E. Simion, "Low level NO_2 detection under humid background and associated sensing mechanism for mesoporous SnO_2," *Sensors and Actuators B: Chemical*, vol. 231, pp. 166-174, 2016.
- E. Ogel, S. A. Müller, A. Sackmann, F. Gyger, P. Bockstaller, E. Brose, M. Casapu, L. Schöttner, D. Gerthsen, C. Feldmann and J.-D. Grunwaldt, "Comparison of the catalytic performance and carbon monoxide sensing behavior of Pd-SnO_2 core@shell nanocomposites," *ChemCatChem*, vol. 9, no. 3, pp. 407-413, 2017.
- T. Suzuki, F. Lauxmann, A. Sackmann, A. Staerz, U. Weimar, C. Berthold and N. Barsan, "Operando Investigations of Rare-Earth Oxycarbonate CO_2 Sensors," *Proceedings*, vol. 2, no. 13, MDPI, 2018.

- A. Stanoiu, C. E. Simion, A. Sackmann, M. Baibarac, O. G. Florea, P. Osiceanu, V. S. Teodorescu and S. Somacescu, "Networked mesoporous SnO_2 nanostructures templated by Brij® 35 with enhanced H_2S selective performance," *Microporous and Mesoporous Materials*, vol. 270, pp. 93-101, 2018.
- Z. Wang, A. Sackmann, S. Gao, U. Weimar, G. Lu, S. Liu, T. Zhang and N. Barsan, "Study on highly selective sensing behavior of ppb-level oxidizing gas sensors based on Zn_2SnO_4 nanoparticles immobilized on reduced graphene oxide under humidity conditions," *Sensors and Actuators B: Chemical*, vol. 285, pp. 590-600, 2019.
- T. Suzuki, A. Sackmann, A. Oprea, U. Weimar and N. Barsan, "Rare-earth based chemoresistive CO_2 Sensors," *TRANSDUCERS & EUROSENSORS XXXIII*, Berlin, Germany, pp. 1309-1312, 2019.
- T. Suzuki, A. Sackmann, A. Oprea, U. Weimar and N. Barsan, "Rare-earth based chemoresistive CO_2 sensors and their operando investigations," *Proceedings*, vol. 87, no. 1, MDPI, 2019.
- A. A. Alharbi, A. Sackmann, U. Weimar and N. Barsan, "A highly selective sensor to acetylene and ethylene based on $LaFeO_3$," *Sensors and Actuators B: Chemical*, vol. 303, pp. 127204, 2020.
- T. Suzuki, A. Sackmann, F. Lauxmann, C. Berthold, U. Weimar and N. Barsan, "CO_2 sensing with gas sensors based on rare-earth compounds: Material exploration," *Sensors and Actuators B: Chemical*, vol. 317, pp 128128, 2020.
- T. Suzuki, A. Sackmann, A. Oprea, U. Weimar and N. Barsan, "Chemoresistive CO_2 gas sensors based on $La_2O_2CO_3$: Sensing mechanism insights provided by operando characterization," *ACS sensors*, vol. 5, no. 8, pp. 2555-2562, 2020.
- A. A. Alharbi, A. Sackmann, U. Weimar and N. Barsan, "Essential role of electrode materials in ethylene and acetylene sensing selectivity for $LaFeO_3$ based gas sensors," *Sensors and Actuators B: Chemical*, vol. 353, pp. 131079, 2022.

Oral presentations at conferences:

- A. Sackmann, F. Gyger, M. Hübner, P. Bockstaller, D. Gerthsen, U. Weimar, N. Barsan and C. Feldmann, "Position effect of Pd additives on the detection of reducing gases for nanoscale SnO_2 hollow sphere based gas sensors," 9-12 September, 2012, Krakow, Poland.